PET Image Quality in the Vicinity of the Bladder with Fluorine-18 and Gallium-68

by

Chenjie Zhang

Graduate Program in Medical Physics
Duke University and Duke Kunshan University

Date: _____

Approved:

_____
Timothy G. Turkington, Supervisor

_____
James E. Bowsher

_____
Terence Z. Wong

Thesis submitted in partial fulfillment of the requirements for
the degree of Master of Science in the Graduate Program
in Medical Physics in the Graduate School of
Duke University and Duke Kunshan University
2018

Abstract

PET Image Quality in the Vicinity of the Bladder with Fluorine-18 and Gallium-68

by

Chenjie Zhang

Graduate Program in Medical Physics
Duke University and Duke Kunshan University

Date: _____

Approved:

_____
Timothy G. Turkington, Supervisor

_____
James E. Bowsher

_____
Terence Z. Wong

An abstract of a thesis submitted in partial fulfillment of the requirements for the degree of Master of Science in the Graduate Program in Medical Physics in the Graduate School of Duke University and Duke Kunshan University
2018

Abstract

Gallium-68 labeled compounds have an important role in the PET imaging of detecting neuroendocrine tumors and prostate tumors. As the prostate exists near the bladder, image quality of prostate tumors can be challenged by radioactivity concentration accumulated in the bladder. Previous studies have shown that activity measurements within 4 cm distal to the bladder were more affected by its higher ^{18}F concentration and improved with the time of flight (TOF) technique. The aim of this research is to understand and compare the effects of ^{68}Ga and ^{18}F activity concentration on evaluation of structures closer to the bladder, and compare it for different scanners, acquisition modes and reconstruction techniques.

Methods: A bladder insert was placed in the center of an oval phantom with radioactivity at three different bladder-to-background ratios: 1:1, 40:1 and 80:1. Twelve 1-cm spheres representing 8:1 small lesions were symmetrically located in two axial planes, all with 1.2 cm distance to the bladder surface. The whole phantom was scanned on both the GE Discovery 690 (D690) and GE Discovery IQ (DIQ), filled with ^{18}F and ^{68}Ga separately. In addition to default reconstruction settings, images were also reconstructed with non-TOF OSEM and TOF OSEM modes on D690, as well as non-TOF OSEM and regularized (REG) modes on DIQ. The same ROIs were applied to all these images.

Results: Radioactivity in the bladder resulted in worse visualization and quantitation of the small spheres. The value difference among the 12 spheres became

greater, and the lesion-to-background ratio were also affected by high bladder activity. The lesion value could be overestimated to be about three time as much as, or underestimated by at most 50% of its true measurement. The greatest difference was seen when the bladder was filled with ^{68}Ga. Both TOF and REG modes provided better lesion value variations compared with non-TOF OSEM reconstruction. Image contrast was significantly improved with more iterations.

Conclusions: Radioactivity of ^{68}Ga in the bladder has a similar but more serious effect than ^{18}F in the value measurements of surrounding structures. Greater measurement variations occur with higher bladder activity concentration. Iterative reconstruction with TOF information or REG reconstruction can be used to improve image quality, otherwise more iterations are recommended.

Dedication

I would like to express my greatest gratitude to my Dad and Mom for their love and financial support that put me through the best education possible.

Also, thank you, Xiaoyan, for keeping me accompanied, shedding lights on my loneliest night and regaining my power until the very end.

Contents

List of Tables

List of Figures

List of Abbreviations and Symbols

Abbreviations

BLAD1	The bladder-to-background ratio of 1.
BLAD40	The bladder-to-background ratio of 40.
BLAD80	The bladder-to-background ratio of 80.
CENT	Bladder in the center.
CT	Computed Tomography.
D690	Discovery 690.
DIQ	Discovery IQ.
DOUB	Combined bed position.
EDGE	Bladder on the edge.
LBG	Large Background ROI.
nTOF	OSEM without Time of Flight.
OSEM	OSEM algorithm in DIQ.
PET	Positron Emission Tomography.
REG	Q.Clear algorithm in DIQ.
SBG	Small Background Region.
SL	Small Lesion.
TOF	OSEM with Time of Flight.

Acknowledgements

I first would like to thank my supervisor Dr. Timothy Turkington for his unwavering support and mentorship. I could never have done this without his passionate teaching and guidance. Thank Robin Davis for offering help in phantom filling and setup, as well as watching ^{68}Ga elution in the Duke Medical Center Radiopharmacy. Thanks to the rest staff in the Duke PET facility for their assistance during my observation of PET scan and image interpretation. At last, I would like to thank Dr. Yin and other faculty in this program that helped with my study and life when I was in Durham.

1

Introduction

1.1 PET/CT

Positron Emission Tomography/Computed Tomography (PET/CT) is a nuclear medicine imaging technique that provides co-registered anatomical and functional images in one scanning session with positron-emitting radionuclides.

1.1.1 The history of PET

In the 1950s William Sweet and Gordon Brownell reported on a positron scanner at the Massachusetts General Hospital for the localization of brain tumors [1]. This scanner was composed of two sodium iodide (NaI) detectors moving in a rectilinear fashion. Later in the 1960s, Rankowitz *et al.,* used a stationary circular array of 32 scintillation detectors instead to get more information in less time [2]. A clinically applicable PET whole-body camera was developed by Ter-Pogossian, Phelps, Hoffman and Mullani from Washington University in the 1970s [3, 4]. It was not until an alternative to NaI crystal, bismuth germanite (BGO), was found that PET scanner became commercially available [5]. BGO has a greater density and effective atomic number, thus it provides a much higher detection efficiency compared to NaI crystal

of the same size. In 2000 the work of David Townshend *et al.,* resulted in the development of the first combined PET/CT scanner which provided anatomical structures and a faster attenuation correction [6]. Currently PET scanners are always sold in the combination of PET and CT systems.

1.1.2 Overview

PET has advantages compared to CT and MRI to the extent that it provides functional images showing the body's metabolism with the help of varying radiotracers. The radiopharmaceuticals used in PET are analogous to biological molecules (like carbohydrates, proteins and nucleic acids) that participate in many physiological activities. These analogs labeled with positron-emitting radioisotopes (such as ^{11}C, ^{13}N, ^{15}O, ^{18}F and ^{68}Ga) are transported into and accumulate inside target cells via different pathways. These processes are revealed through the detection of emitted radiation in PET scanners.

Positrons from radionuclide decays interact with electrons and produce two 511 keV photons through mutual annihilation. Two annihilation photons are emitted in approximately opposite directions from the site of the annihilation event. They can be nearly simultaneously detected by annihilation coincidence detection (ACD) system, and thus a line of response (LOR) showing their path are recorded in the system. (Fig. 1.1)

1.2 Reconstruction

Image reconstruction is a process that generates images based on digital data (e.g. projection and sinogram data) acquired from imaging modalities. Reconstruction method is one of factors that determine PET image quality. Different parameters of these method have great impacts on reconstructed image quality. Each method has its pros and cons, so that there is no reconstruction method perfectly suitable to

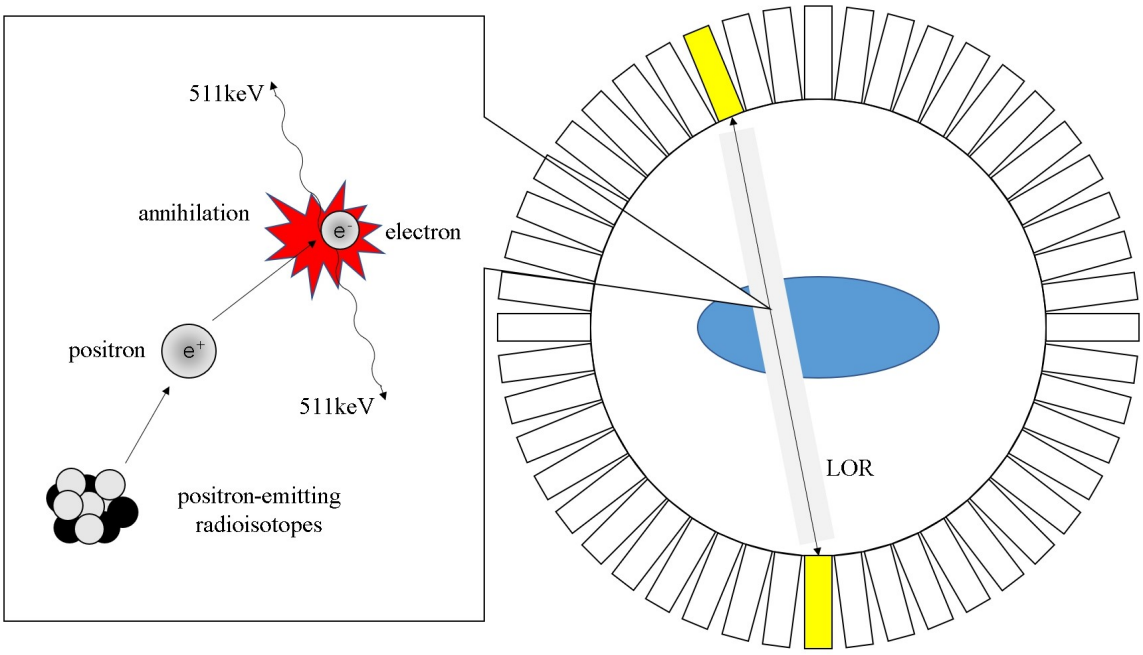

FIGURE 1.1: Illustrations of radioisotope decay and annihilation, and two annihilation photons captured by opposite PET scanners.

all the clinical situations.

1.2.1 Iterative Reconstruction

Filtered Backprojection (FBP) was the first algorithm to be used widely in commercial PET/CT scanners. It is a linear algorithm, meaning that each pixel is a linear function of measured projection values. Iterative reconstruction algorithm is an alternative to FBP in PET imaging reconstruction. Although the iterative method incorporates all corrections, it is computationally more intensive and time-consuming, and thus not until the development of fast computer technology was it prevalent in clinic. The major difference from FBP is that iterative reconstruction uses forward projection. Iterative reconstruction starts with an image estimate which is often very simple. Simulated projections (sinogram) are computed from this image estimate using forward projection and compared with the measured projections (sinogram) from actual image. If they do not agree, the differences can be used to

update the image estimate gradually closer to an image that meets some convergence criteria. [7]

Reconstructed image quality was significantly improved after the expectation maximization (EM) algorithm came out in 1977 by Dempster *et al.* [8]. The EM algorithm provides statistically valid reconstructions by giving more weight to high-count elements and less weight to low-count portions of a profile, while backprojection algorithm offers an equal weight factor. Not until 1994 was Ordered Subsets Expectation Maximization (OSEM) introduced for the purpose of faster reconstruction. [9] In this method all the projection profiles are divided into subsets and only the projections in designated subsets are used at image update. This requires less computational time because the time is proportional to the size of projection profiles included in each iteration. OSEM algorithm, however, is limited to a few iterations because the resolution increases with more iterations at the cost of excessive noise. The potential introduction of distortions in small objects also occurs with less iterations [10].

1.2.2 Time of Flight

Time of Flight (TOF) is a technique that approximately determines the site of annihilation along the LOR by utilizing the difference in time (Δt) at which annihilation photons are detected by two ACD detectors. The distant (Δd) with respect to the midpoint within the LOR can be calculated by

$$\Delta d = \frac{c \times \Delta t}{2}, \tag{1.1}$$

where c is the light velocity (3×10^8m/sec). Although electronic circuits are able to measure infinitesimally short time difference, it is the properties of scintillator crystals and the light readout that determine the accuracy of TOF method used in most modern PET systems. [7]

1.2.3 Bayesian/Penalized Method

A particular Bayesian penalized likelihood reconstruction algorithm called Q.Clear has been implemented new generation of PET/CT scanners from GE. It includes a penalty term which is used for noise control. The PL objective function is:

$$\widehat{x} = arg\ max_{x \geqslant 0} \sum_{i=1}^{n_d} y_i log[Px]_i - [Px]_i - \beta R(x).$$

The first several parts in this equation are the same as in the OSEM algorithm, but are less important in this research and will not be discussed here. $R(x)$ is a penalty function utilizing the difference between neighboring voxels and a function of their sum. β is a penalization factor. They together act as a penalty term to suppress the image noise. When image noise increases, the penalty term increases as well to reduce the objective function during each iteration, and thus preventing the result from noisier images. It allows Q.Clear algorithm to achieve a convergence that avoids high noise, depending on the choice of β, whereas, OSEM reconstruction has to be stopped after a few iterations to prevent image noise increasing. [10]

1.3 Radiopharmaceutical

1.3.1 Fluorine-18-FDG

Fluorine-18

^{18}F is mainly produced using cyclotron via ^{18}O(p, n)^{18}F and ^{20}Ne(d, α)^{18}F reactions. It decays to stable Oxygen-18 by positron emission 96.7% of the time with a half-life of 109.77 minutes (Fig. 1.2). The initial positron mean energy is 250 keV. [7]

FDG

The synthesis of 2-fluoro-2-deoxy-D-glucose (FDG) was first described in 1969 [11]. Later in 1978, Tatsuo Ido and Al Wolf described the synthesis of FDG labeled with ^{18}F [12], which has become the most widely used radiotracer today. ^{18}F-FDG has the similar metabolic pathway in human body of glucose. Most malignant tumor cells express higher affinity for glucose than normal cells, so more glucose and its analog accumulate in tumor cells. ^{18}F-FDG entering a cell is phosphorylated into ^{18}F-FDG-6-phosphate and can no longer be degraded via the glycolysis pathway or dephosphorylated. The more ^{18}F-FDG-6-phosphate trapped in cells, the higher uptake inside the tumor we can observe from PET/CT.

1.3.2 Gallium-68 labeled radiotracers

Gallium-68

^{68}Ga is the product of its parent radionuclide Germanium-68 via electron capture with a half-life of 271 days. ^{68}Ga has a half-life of 67.71 minutes and decays to stable Znic-68. This process (Fig. 1.2) involves 89% positron branching accompanied by high-energy photon emission (the most prominent of which is 1077keV, 3.3%). The initial energy of positron emitted from ^{68}Ga is 836 keV on average which is much higher than that from ^{18}F. [7]

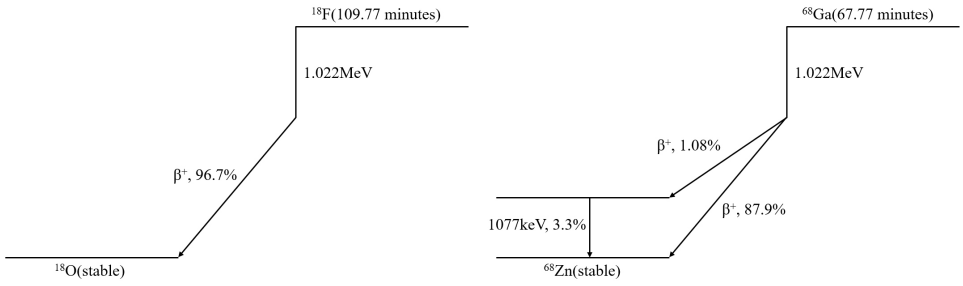

(a) ^{18}F-^{18}O (b) ^{68}Ga-^{68}Zn

FIGURE 1.2: Simplified Illustration of ^{18}F and ^{68}Ga Decay

DOTA Compounds

It was a great improvement for PET Radiopharmacy after the introduction of 1,4,7,10-tetraazacyclododecane-1,4,7,10-tetraacetic acid (DOTA). ^{68}Ga labeled peptides have been proven to be superior to other radiotracers in recent decades [29], and DOTA-Tyr3 octreotate (DOTA-TATE) is one of these new compounds that is adopted in the Duke University Medical Center (DUMC) PET Facility.

DOTA is an organic compound acting as a chelator that can be linked to molecules which have affinity for various structures. DOTA was first synthesized in 1976 from cyclen and bromoacetic acid [14]. This method is simple and still in use [15]. DOTA-TATE is an amide of the acid DOTA and Tyr3-octreotate. Tyr3-octreotate is a derivative of octreotide that binds to somatostatin receptors (SSTRs). SSTR is the membrane-bound receptor presented in normal human tissues, such as spleen, kidneys, adrenal glands, liver and brain [16, 17, 27]. It is also abundant in a variety of human neuroendocrine tumor (NET) cells, which are target cells for somatostatin analogs in imaging or treatment. The ^{68}Ga labeled peptides show a rapid renal clearance and are rapidly accumulated in the tumors, while the concentration in tissues without expression of SS receptors is low, providing better target contrast [19].

1.4 Research Aim

Reduced image quality occurs in the vicinity of the bladder when its radioactivity is high. Evaluation of potential prostate, uterus, rectum tumors and pelvic lymph node metastases will be influenced, because these tumors usually exist near the bladder. Even though patients are asked to void before the scan, bladders still can have the highest radioactivity during the PET acquisition [27]. Allen *et al.,* have studied the effect of ^{18}F-FDG bladder radioactivity on its surroundings. They

concluded that lesions less than 4 cm distal to the bladder showed more variability but imaging was improved with TOF PET reconstruction, and the lesion measurements became more accurate with lower radioactivity in the bladder [21].

Several studies have shown the more and more important role of ^{68}Ga in medical imaging of prostate including primary, recurrent tumors and metastases [22–24]. ^{68}Ga and ^{18}F have different preferences for detecting tumors, however, they have the same property of high bladder radioactivity. Compared to ^{18}F, the effect of ^{68}Ga bladder radioactivity on its surrounding structures is still unknown. It is meaningful to understand how much changes in the vicinity of the bladder are related to its radioactivity. It is also the main interest of this research. Other factors taken into consideration include bed positions, choices of radionuclide and machine, as well as reconstruction parameters.

We have performed a phantom study to evaluate image quality in the vicinity of high-uptake bladder using ^{18}F and ^{68}Ga and a variety of acquisition modes and image processing parameters.

2

Materials & Methods

2.1 Equipment

2.1.1 Phantom

1. The bladder insert was a 100 ml sphere (of 58 mm inner-diameter) with two threaded holes on the top and bottom sides. Holes were connected to the front side of the oval phantom with two tubes for the purpose of injecting and removing radioactivity. The bladder insert was attached to a PVC threaded rod on a perpendicular insert in order to be vertically and horizontally centered (Fig. 2.1).

2. Twelve small spheres (0.5 ml, of 1 cm inner-diameter each) were attached to 12 chemical-resistant PVC threaded rods with 1.2 cm away from the bladder surface. Eight of them were in the mid-transverse plane of the bladder, and other 4 spheres were in another transverse plane which was near the edge of the bladder (Fig. 2.2).

3. An oval phantom, 40 cm × 36 cm × 21 cm (length × major axis × minor axis), was used to simulate abdomen (Fig. 2.3). An insert was connected to the back

FIGURE 2.1: The bladder insert was vertically and horizontally centered on a perpendicular insert, twelve lesions were also symmetrically placed (only 8 spheres could be seen above).

side of the phantom to hold the bladder and surrounding lesions. The bladder was centered on the insert, and 12 lesions were symmetrically placed (Fig. 2.4).

2.1.2 Scanner

All phantoms were scanned by the GE Discovery 690 (D690) and Discovery IQ (DIQ) PET/CT systems at the DUMC PET Facility. The D690 PET/CT system consists of a 24-ring Lutetium Yttrium Orthosilicate (LYSO) PET system and a 64-slice CT system. Each individual LYSO crystal has a dimension of 4.2 × 6.3 × 25 mm^3 (circumferential × axial × radial) and every 54 (9 × 6, circumferential × axial) crystals are grouped into blocks. Hence, there are 4 block rings which have 64 detector blocks per block ring, and in total 13,824 individual LYSO crystals. [25] The DIQ PET/CT system is a 5-ring Bismuth Germanium Oxide (BGO) PET system and

(a) Front View (b) Top View

FIGURE 2.2: Twelve lesions were placed on a perpendicular insert: No.1-8 and No. 9-12 were in two different axial planes.

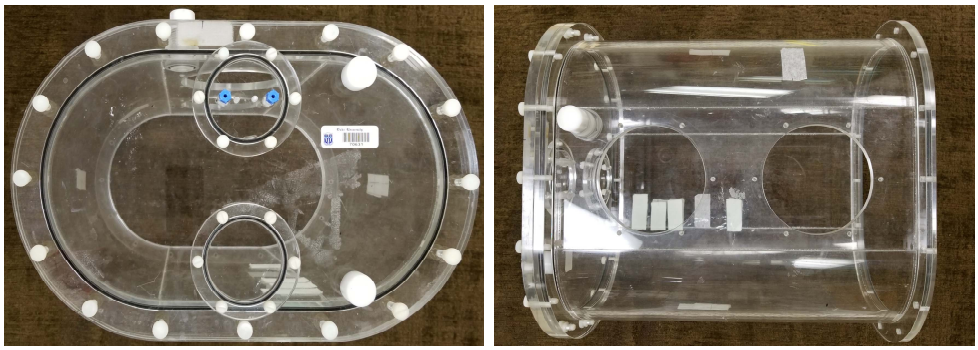

(a) Front View (b) Top View

FIGURE 2.3: The oval phantom

a 16-slice CT system. There are 36 detector units per block ring with BGO crystals of $6.3 \times 6.3 \times 30\ \text{mm}^3$ (circumferential $\times$ axial $\times$ radial) and the coincidence window of 9.5 ns. [26]

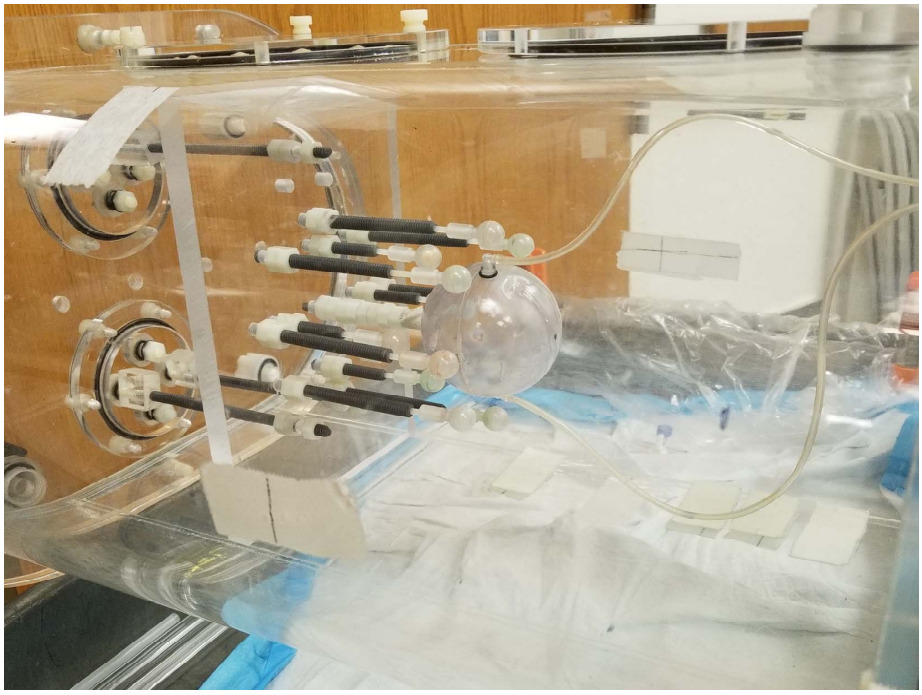

FIGURE 2.4: The completed torso phantom setup. A perpendicular insert connecting to the back side of the phantom held the bladder and 12 lesion inserts, two tubes was connected to the front side.

2.2 Default Setting Studies

The following studies were based on reconstructed images acquired from default OSEM setting on D690 and DIQ. Default OSEM settings were 2 iterations × 16 subsets × 6.4 mm filter cutoff on D690 (slightly different from what is adopted at DUMC) and 4 iterations × 12 subsets × 6.4 mm filter cutoff on DIQ. For better comparison, 'nTOF' was used to represent the OSEM algorithm on D690.

2.2.1 Bladder Concentration Level Studies

Three different bladder activity concentration levels were studied: the bladder-to-background activity ratios were 1:1 (BLAD1), 40:1 (BLAD40) and 80:1 (BLAD80). The three levels could be achieved during the PET scan without changing the phantom setup and therefore utilizing the same CT data for attenuation correction. The

bladder was originally filled with background solution to achieve BLAD1 condition. After the first scan, the bladder was emptied and filled again with high activity solution (BLAD80 scan). At last, half of the bladder volume was replaced by radioactivity-free water to reduce its concentration for BLAD40 scan.

2.2.2 Bed Position Studies

This was a small study to see the effect of relative position of the bladder to detectors. The whole phantom was scanned with two bed positions, bladder in the center (CENT) and in the edge (EDGE). In addition, images were reconstructed not only with the above individual bed positions, but also, under the default setting, with data combined from both positions (DOUB).

2.2.3 Radionuclide Studies

The effect of ^{18}F was compared to ^{68}Ga for this research. In this case, all the studies mentioned above and below with ^{18}F were repeated with ^{68}Ga in another day.

2.2.4 Algorithm Comparison Studies

Two choices are available using the D690 PET/CT console: the VUE Point HD uses fully 3D OSEM algorithm (nTOF), and the VUE Point FX incorporates OSEM algorithm with TOF technique (TOF). The DIQ PET/CT system includes two algorithms, 3D-OSEM which is the same with D690 (OSEM) and Q.Clear that has only one parameter, penalty term β (REG). The phantom underwent scans separately on two PET scanners, and data acquired were reconstructed with two choices available on each machine.

2.3 Data Acquisition

The phantom was set up for the DUMC "skull-base to mid-thigh" (SBMT) protocol with all corrections. The torso phantom was first filled to half of its volume

with room temperature water. The 1-cm spheres were filled with the diluted activity together with CT contrast (3% oral iodine) to achieve the lesion-to-background ratio of 8:1. The rest of water containing radioactivity was added into the phantom after 12 lesions were screwed on the rods. The bladder insert was next filled with the solution from the torso phantom to achieve a 1:1 bladder-to-background activity ratio.

A fast CT scout was performed at first, and based on that, the scan range was established to collect data from two bed positions. The full CT scan was then performed for attenuation correction purpose, followed by 3D-mode PET acquisition. 4-minute scan time was required for each bed position. The detailed process of obtaining data from three concentration levels are shown in the section 2.2.1.

2.4 Reconstruction Setting Studies

2.4.1 Discovery 690 Setting Studies

Image data acquired from D690 PET/CT scanner were reconstructed to create 256 × 256 × 47 voxel images for the CENT and EDGE position, and 256 × 256 × 71 for the DOUB position, resulting in each voxel size of 1.95 mm × 1.95 mm × 3.27 mm. Besides the default setting mentioned in the section 2.2, the following parameters were only applied to CENT data sets:

- 3, 4, 6, 10 and 20 iterations separately × 12 subsets × 6.4 mm filter cutoff.

2.4.2 Discovery IQ Setting Studies

Similarly, data acquired from DIQ were reconstructed into 256 × 256 × 79 matrices and 256 × 256 × 119 matrices depending on the number of bed positions involved. Individual voxel size was 1.95 mm × 1.95 mm × 3.26 mm. In addition to default OSEM mode and REG mode ($\beta = 350$), it was necessary only for the CENT data to be reconstructed in terms of varying parameters:

- 3, 6, 10 and 20 iterations separately × 12 subsets × 6.4 mm filter cutoff.

2.5 Data Analysis

CT image data acquired from either D690 or DIQ were reconstructed into 512 × 512 matrices at first, and then were converted into the same matrix size as PET images (256 × 256) for the purpose of facilitating the analysis of region of interest (ROI). ROIs drawn on CT images were categorized as followed (Fig. 2.5):

1. ROIs (SL01 - SL12) were applied to each lesion over three to four slices by drawing larger ROIs and then limiting by a threshold. The lesion values were higher than background because of the iodine contrast. The threshold was then set based on the maximum value of background and the minimum value of rods. Both the mean and max values were measured for SL ROIs.

2. One ROI (BLADDER) was drawn in a more central region of the bladder over several slices to avoid boundary fall-off effects. The bladder value referred to the mean value over several slices.

3. A large background ROI (LBG) was drawn excluding 12 lesions in each slice with the bladder. The mean value of the background for each image set was determined by averaging all LBGs slice to slice.

4. Twelve small background ROIs (SBG01 - SBG12) with the same size of lesions were applied between each two lesions and had the same distance from the surface of bladder. The mean value for each SBG was collected by averaging all voxel values in one ROI.

(a) Mid-Axial Plane

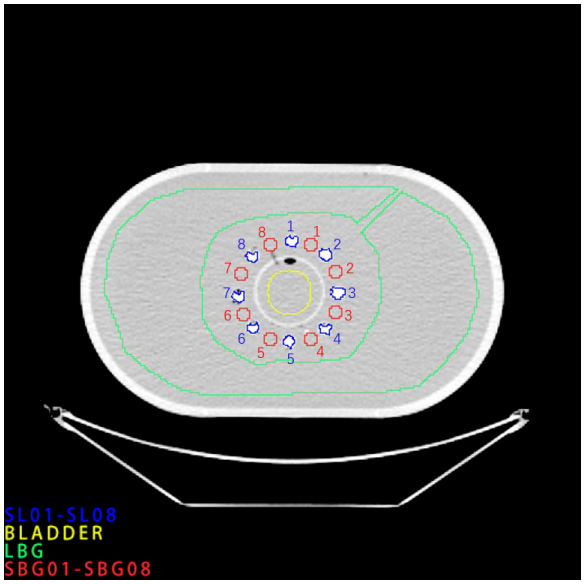

(b) Bladder-Edge Axial Plane

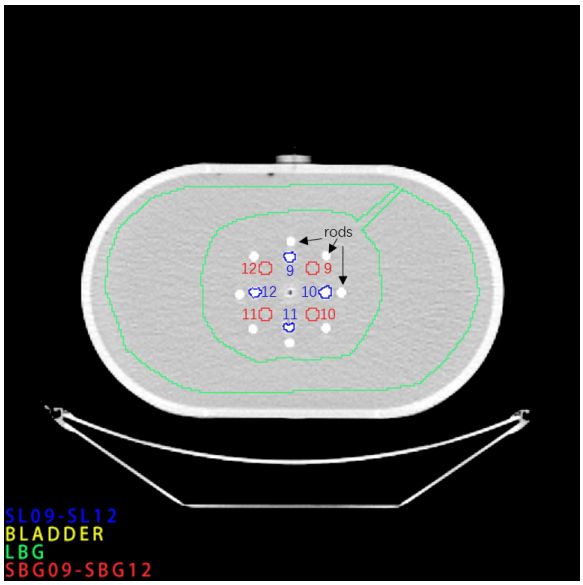

FIGURE 2.5: Illustration of ROIs drawing. The black regions inside the phantom were air bubbles. (a) shows SL01 - SL08, (b) is from SL09 to SL12.

3

Results

3.1 Default Setting Results

3.1.1 Bladder Concentration Level Results

Fig. 3.1 compares different bladder concentration for each study. Each row is one study and each column represents one bladder activity level. Twelve lesions were all affected. Analyses for data reconstructed with default D690 nTOF (or DIQ OSEM) algorithm are displayed via line charts in Fig. 3.2 to 3.9. The x-axis represents the number of lesions (SL01 - SL12) or background ROIs (SBG01 - SBG12) in the vicinity of the bladder. The y-axis represents lesion radioactivity concentration that was normalized to its corresponding BLAD1 scan (also was control group) for respective machine and radionuclide (D690 F18 or DIQ Ga68, i.e.), and thus a line of value = 1 means lesion radioactivity concentration for BLAD1 scan was normalized to itself for comparative purpose.

The relative activity difference results are shown in Fig. 3.10, the x-axis represents four combinations of scanner and algorithm. The y-axis is the sum of absolute value of normalized differences between hot bladder scans (BLAD40 and BLAD80) and control group. It is applied to both lesion and background ROIs studies.

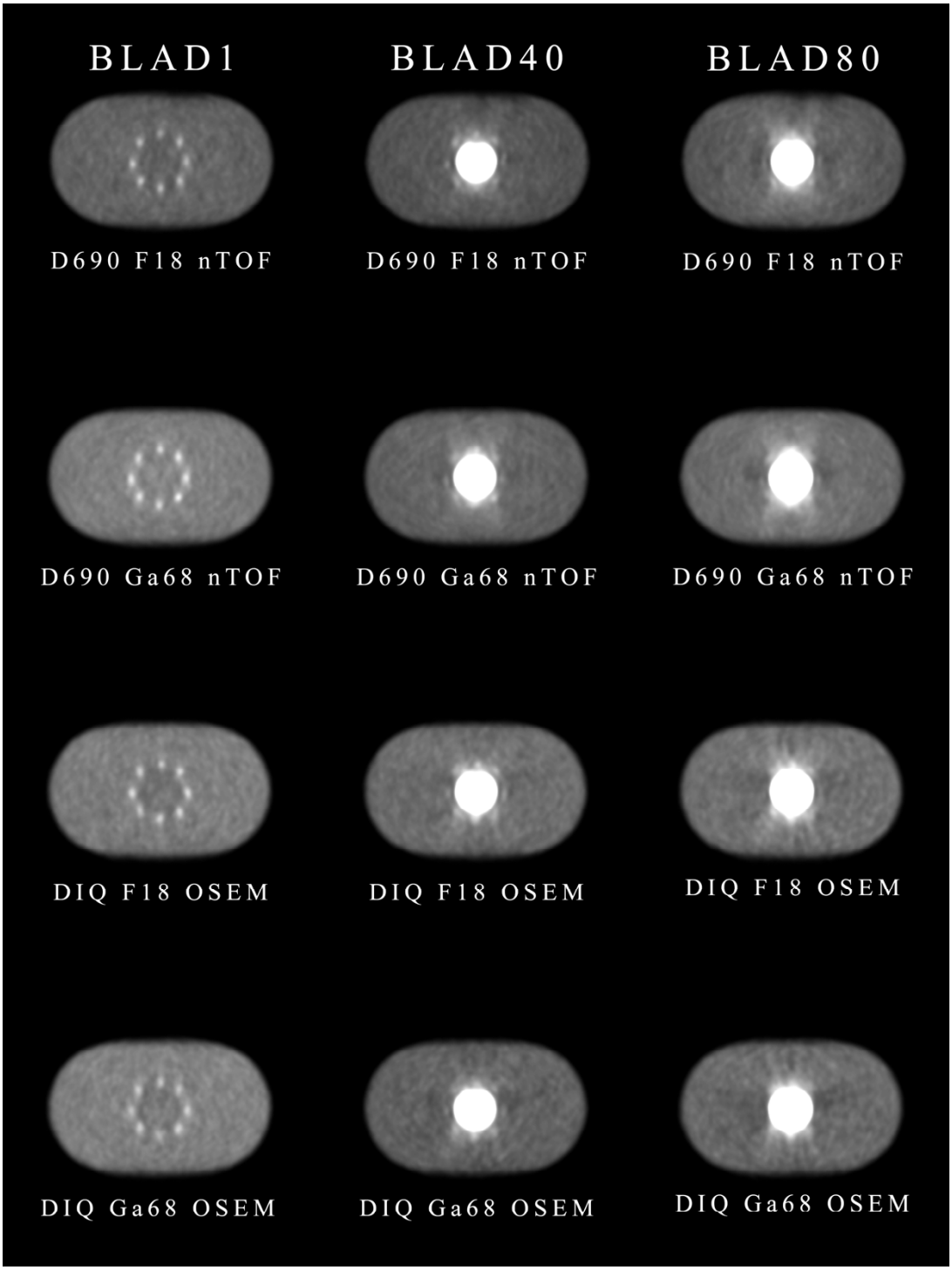

FIGURE 3.1: Results for default nTOF (or OSEM) settings. Each row represents one combination of machine, isotope and reconstruction, each column is one bladder concentration level. Bladder activity concentration significantly affected 12 lesions around it.

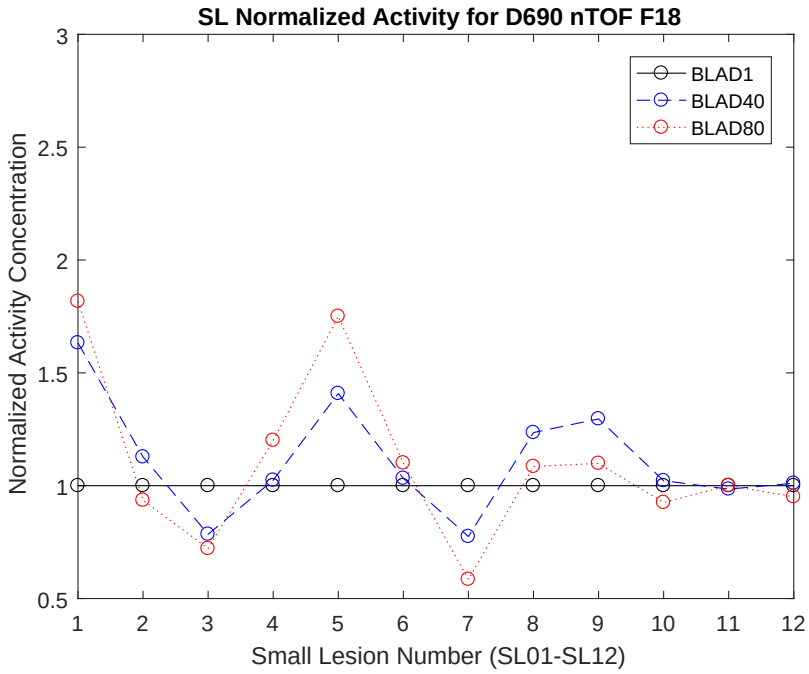

FIGURE 3.2: Normalized activity concentration to its corresponding BLAD1 scan for 12 SL with D690 nTOF F18.

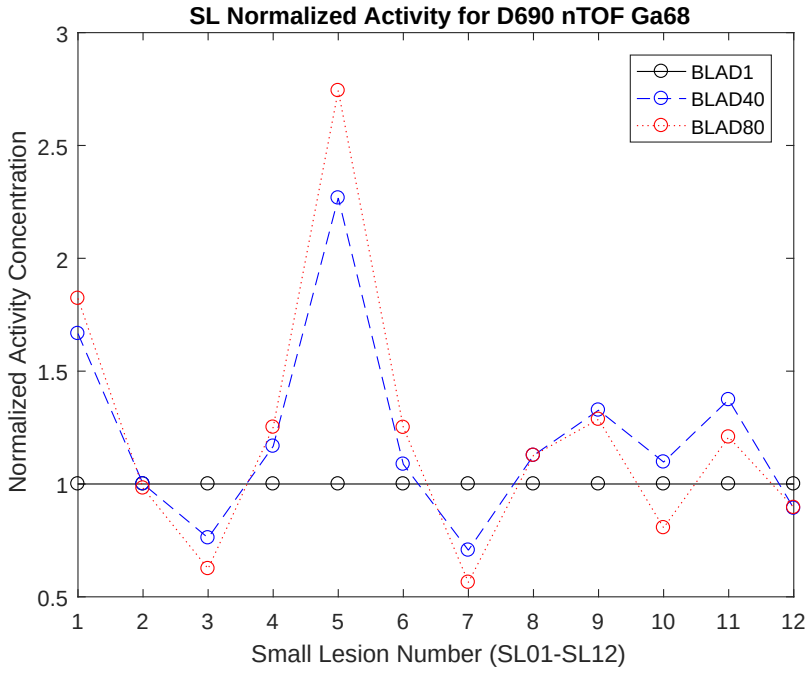

FIGURE 3.3: Normalized activity concentration to its corresponding BLAD1 scan for 12 SL with D690 nTOF Ga68.

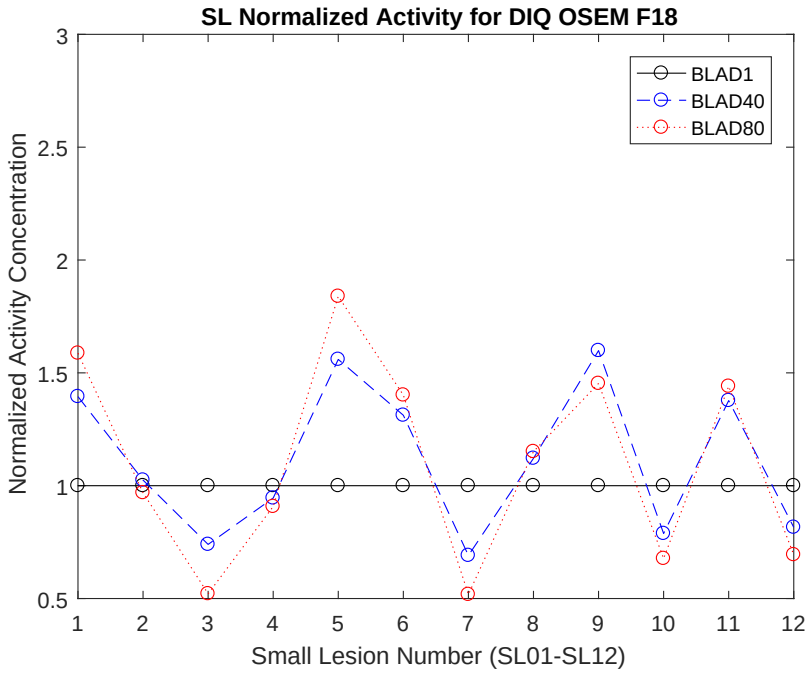

FIGURE 3.4: Normalized activity concentration to its corresponding BLAD1 scan for 12 SL with DIQ OSEM F18.

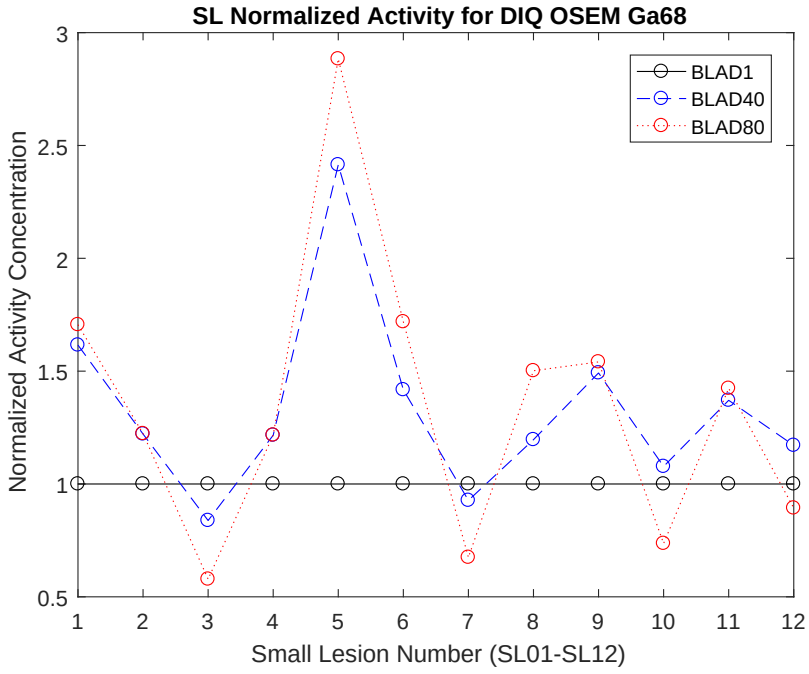

FIGURE 3.5: Normalized activity concentration to its corresponding BLAD1 scan for 12 SL with DIQ OSEM Ga68.

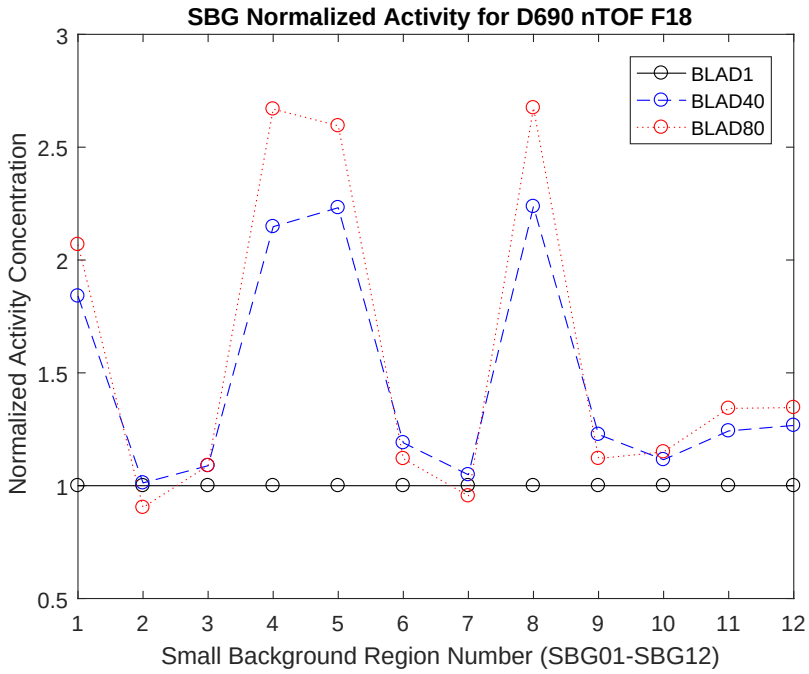

FIGURE 3.6: Normalized activity concentration to its corresponding BLAD1 scan for 12 SBG with D690 nTOF F18.

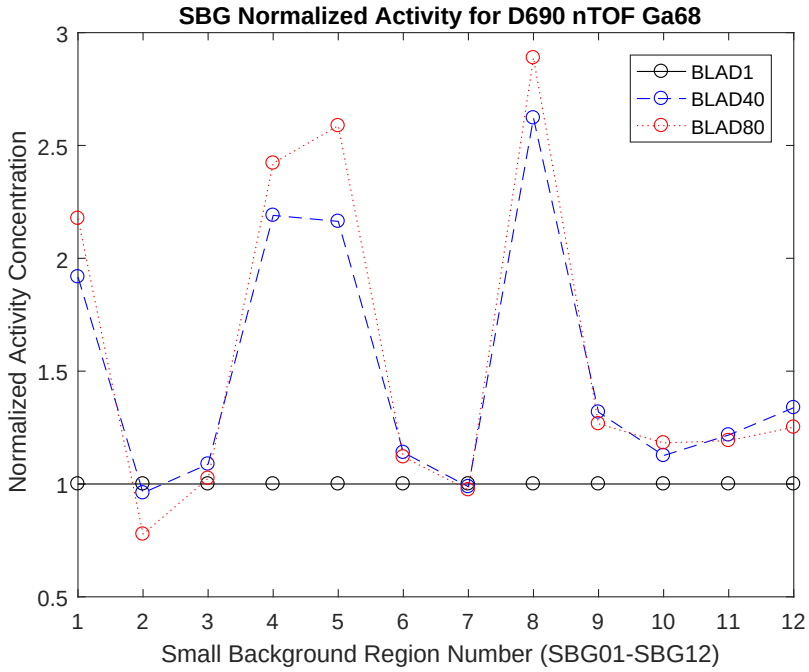

FIGURE 3.7: Normalized activity concentration to its corresponding BLAD1 scan for 12 SBG with D690 nTOF Ga68.

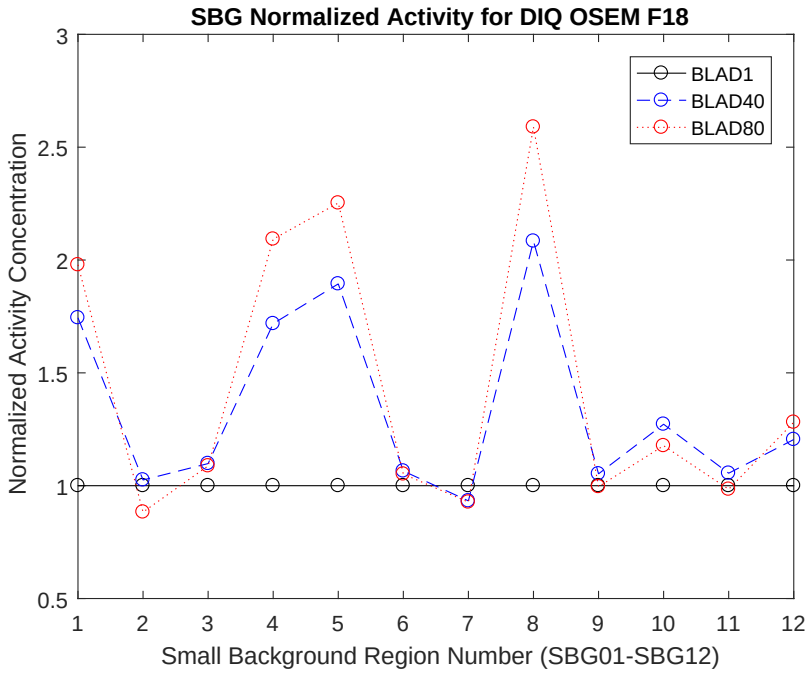

FIGURE 3.8: Normalized activity concentration to its corresponding BLAD1 scan for 12 SBG with DIQ OSEM F18.

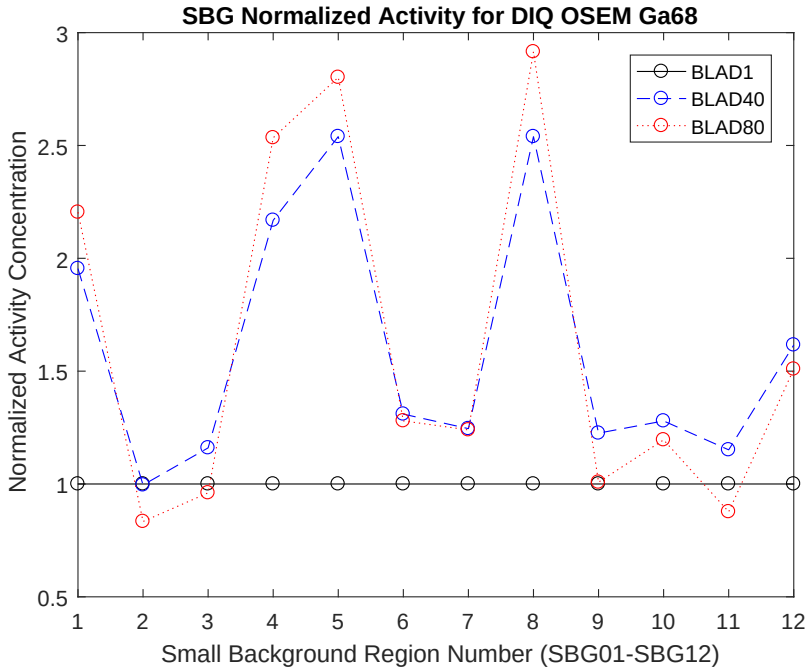

FIGURE 3.9: Normalized activity concentration to its corresponding BLAD1 scan for 12 SBG with DIQ OSEM Ga68.

(a) The Sum of Relative Activity Difference for 12 SL

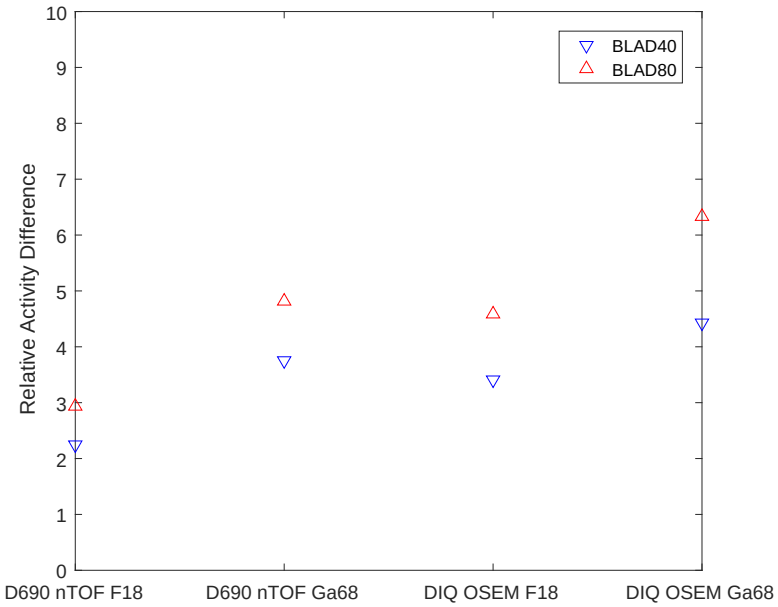

(b) The Sum of Relative Activity Difference for 12 SBG

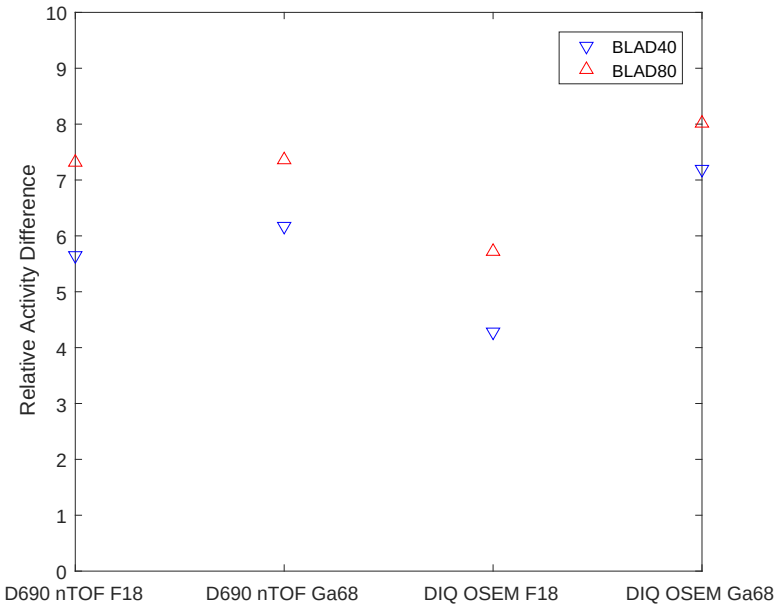

FIGURE 3.10: The sum of relative activity difference for BLAD40 and BLAD80 with different plans in default nTOF (or OSEM) setting. (a) for 12 SL; (b) for 12 SBG.

Four default scans show the same trend on how activity concentrations inside the bladder affect its surroundings based on three concentration levels. The BLAD80 level changes activity concentrations in 12 SL to a much higher extent than BLAD40. Depending on PET scanners and reconstruction algorithms, higher bladder concentration gives rise to higher SL values, e.g. SL05 (Fig. 3.3), up to almost three times of BLAD1 values, and decreases them by half at most, e.g. SL07 (Fig. 3.4). Not only for hot lesions, background areas near the bladder also suffer this effect, which can be seen in Fig. 3.6 to 3.9. On the other hand, Fig 3.10 compares the relative activity concentration difference between BLAD40 and BLAD80 under varying conditions. Greater relative difference indicates more changes that the BLAD80 bladder makes to its surroundings. The effect also applies to other cases.

To simplify results in lesion and background comparison, data are chosen from D690 Ga68 nTOF set. The x-axis still represents the number of lesions (SL01 - SL12) in the vicinity of the bladder. The y-axis in Fig. 3.11a is the activity ratio of each lesion value to LBG value in corresponding image set. The y-axis in Fig. 3.11b is the activity ratio of one lesion value to the average value of its closest two background ROIs in the same image set, e.g., lesion SL01 and ROIs SBG01, SBG08.

Lesion and background comparison shows a similar trend as we discussed above. Basically, the bladder surroundings are more affected by the BLAD80 concentration level. Values of Lesions SL03 and SL07 become smaller while values of SL01, SL05 have significant increments when the bladder concentration is higher. Comparison of Fig. 3.11a to Fig. 3.11b confirms that background value gets higher as it is closer to the bladder, due to the fact that ratios of SL to LBG are greater than SL-to-SBG ratios at the same bladder concentration level for all 12 lesions, and 12 SBG exist closer to bladder surface than LBG.

(a) SL-to-LBG Activity Ratio for D690 nTOF Ga68

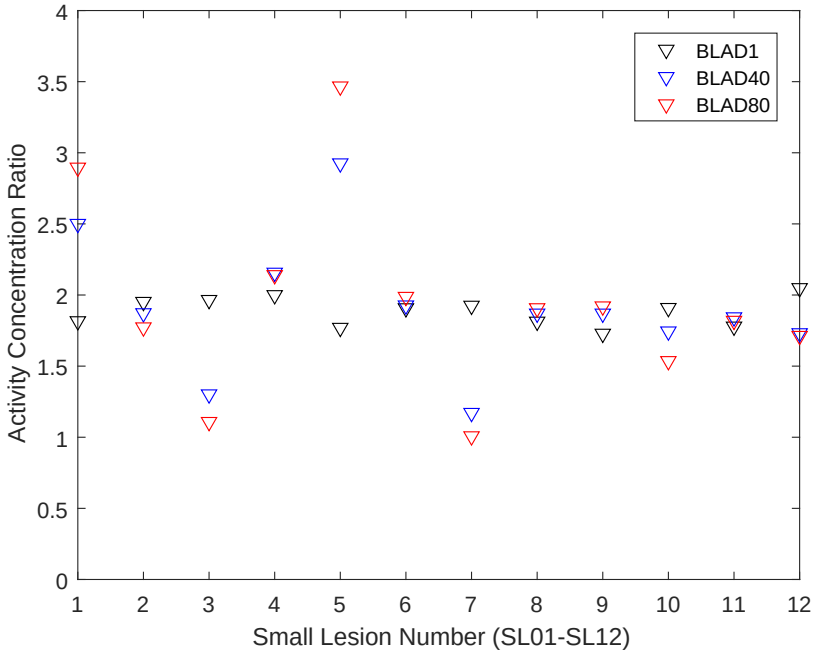

(b) SL-to-SBG Activity Ratio for D690 nTOF Ga68

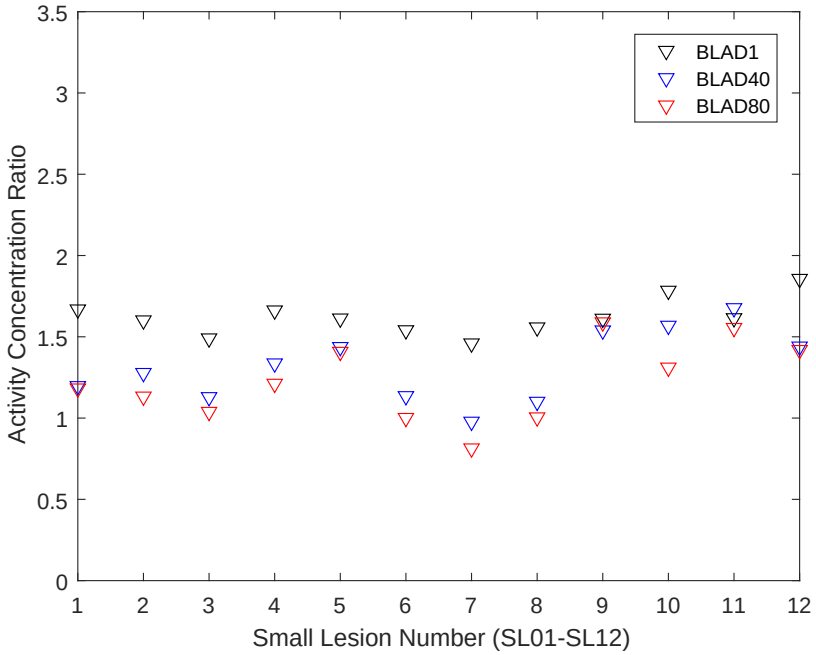

FIGURE 3.11: The ratio of 12 lesions to background in image sets with D690 nTOF Ga68, (a) is the ratio to LBG; (b) is to its two closest SBG.

Lesion-to-background-ROIs results also show that with increased bladder activity concentration, it becomes harder to distinguish hot lesions from the background, and it is even worse for BLAD80 than BLAD40. The activity concentration in each lesion was designed to be 8 times as much as that in the background. When it was displayed after PET scan, however, lesion activity becomes 3.5 times the value of the background. And with increased bladder concentration, it gradually decreases to much less than the background value in the vicinity of the bladder.

3.1.2 Bed Position Results

Comparison of bed positions for D690 Ga68 nTOF is shown in Fig. 3.12. Images displayed in the same window and level are aligned with bladder concentration as row and bed position as column. No obvious difference between CENT and DOUB sets is noticed. Images of bladder in the edge have so much noise that it cannot tell where 12 lesions are. Further quantitative analysis is not included in this study.

3.1.3 Radionuclide Results

The only factor that changed and caused the difference in Fig. 3.2 and Fig. 3.3 is the use of radionuclides (nTOF and OSEM are different names for the same algorithm). The relative increments in SL05 with D690 ^{18}F are 1.4 and 1.8 for BLAD40 and BLAD80, separately. However, they become 2.3 and 2.7 in the same region for the scan with D690 ^{68}Ga. The same phenomenon occurs when scans were performed on DIQ, which can be observed in Fig. 3.4 and 3.5. The sum of relative activity difference (Fig. 3.10) also shows that ^{68}Ga causes more variability in the values of the bladder surroundings than ^{18}F no matter which machine was used. The choice of radionuclides affects the background which is close to the bladder as well. We can see great differences between ^{18}F and ^{68}Ga on DIQ, though on D690, the sum of relative activity is just slightly higher for ^{68}Ga than ^{18}F.

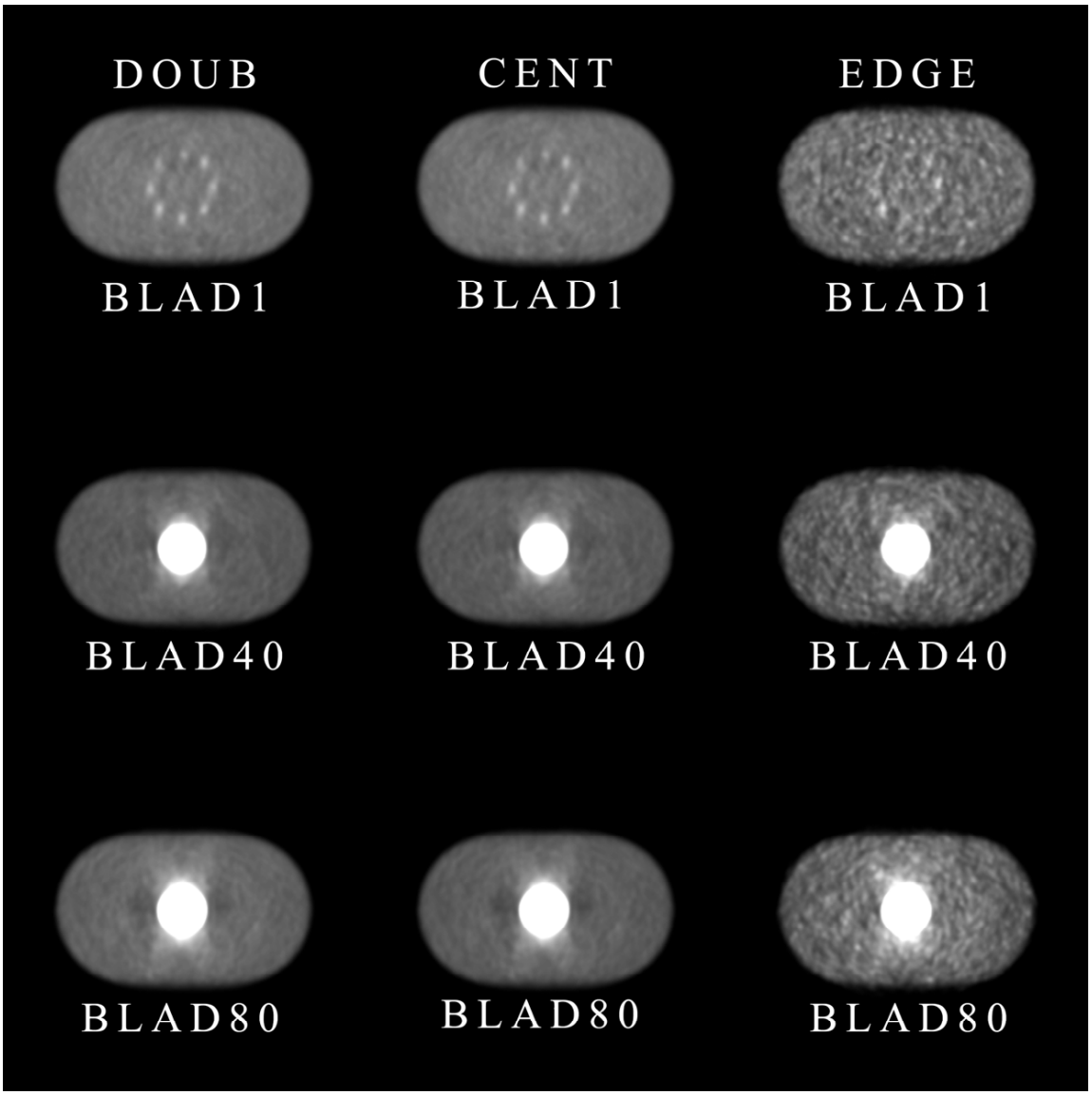

FIGURE 3.12: Images from D690 nTOF Ga68, displayed in bed position vs. bladder concentration. There was no great difference in either bladder or its surrounding lesions between CENT and DOUB positions.

3.1.4 Algorithm Comparison Results

Fig. 3.13 compares different bladder concentration for each study. Each row represents one study including D690 F18 TOF, D690 Ga68 TOF, DIQ F18 REG and DIQ Ga68 REG. The column represents one bladder activity level. Twelve lesions were more affected at BLAD80 than BLAD40, but showed better visualization compared with Fig. 3.1.

Analyses for data reconstructed with default D690 TOF or DIQ REG are displayed to Fig. 3.14 to Fig. 3.21. The x-axis represents the number of lesions (SL01 - SL12) or background ROIs (SBG01 - SBG12) in the vicinity of bladder. The y-axis represents lesion radioactivity concentration that was normalized in the same way of the section 3.1.1. The last one compares the sum of absolute of relative activity difference in SL (3.22a) and SBG (3.22b) with reconstruction settings other than that in Fig. 3.10a but is displayed in the same way.

Normalized activity concentration results show that lesion value changes under TOF and REG modes are considerably lower compared with that under nTOF (or OSEM) mode, separately. In other words, image distortion in the vicinity of the bladder due to its high concentration is getting improved. It is the same for SBG near the bladder that TOF and REG are helpful to reduce the apparently high background value. The sum of absolute of relative activity difference in either SL or SBG shows similar results compared to that with the help of TOF and REG, value variations resulted from relative high bladder activity become smaller under TOF and REG modes.

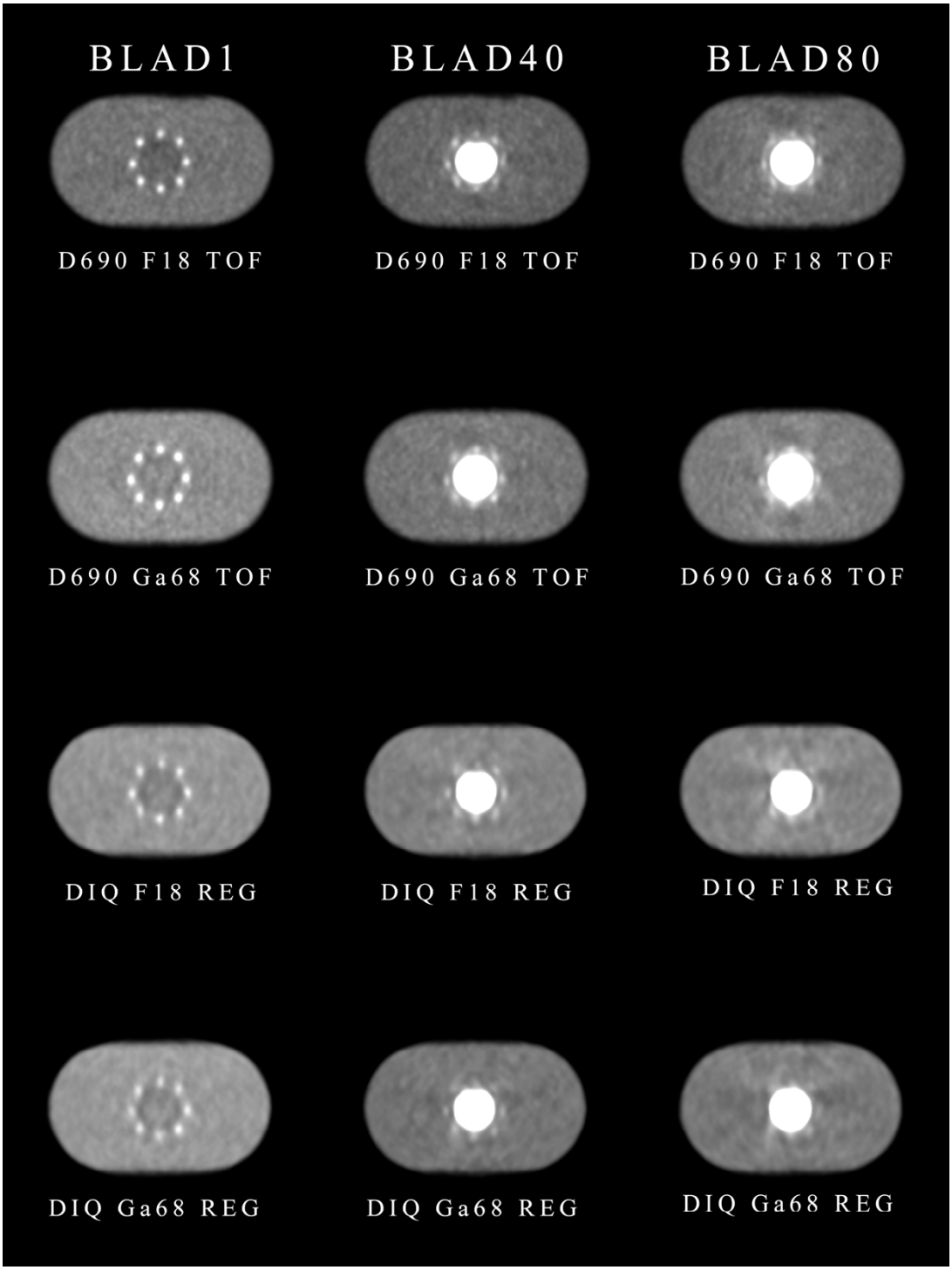

FIGURE 3.13: Results for default TOF and REG settings. Each row represents one combination of machine, isotope and reconstruction, each column is bladder concentration level. Twelve lesions were more affected at BLAD80 than BLAD40.

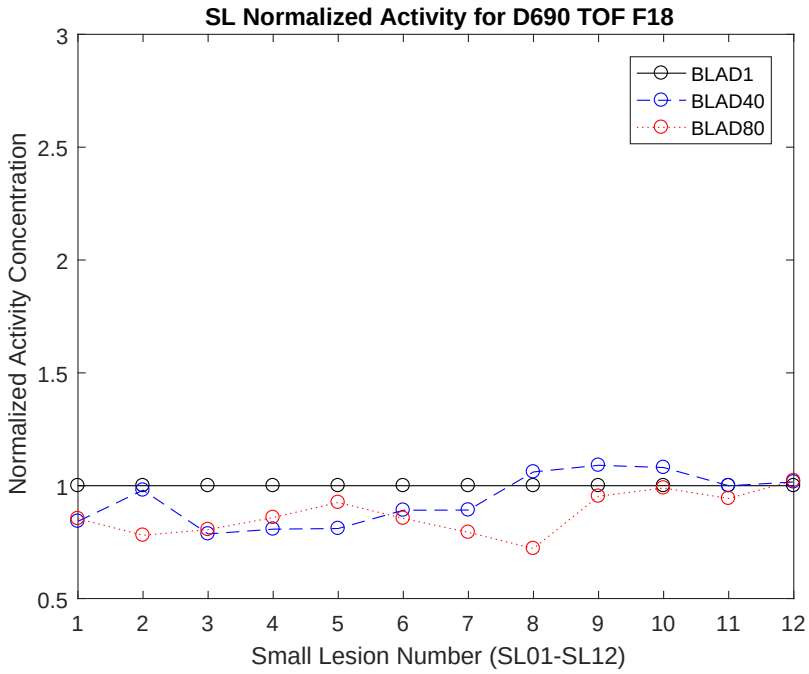

FIGURE 3.14: Normalized activity concentration to its corresponding BLAD1 scan for 12 SL with D690 TOF F18.

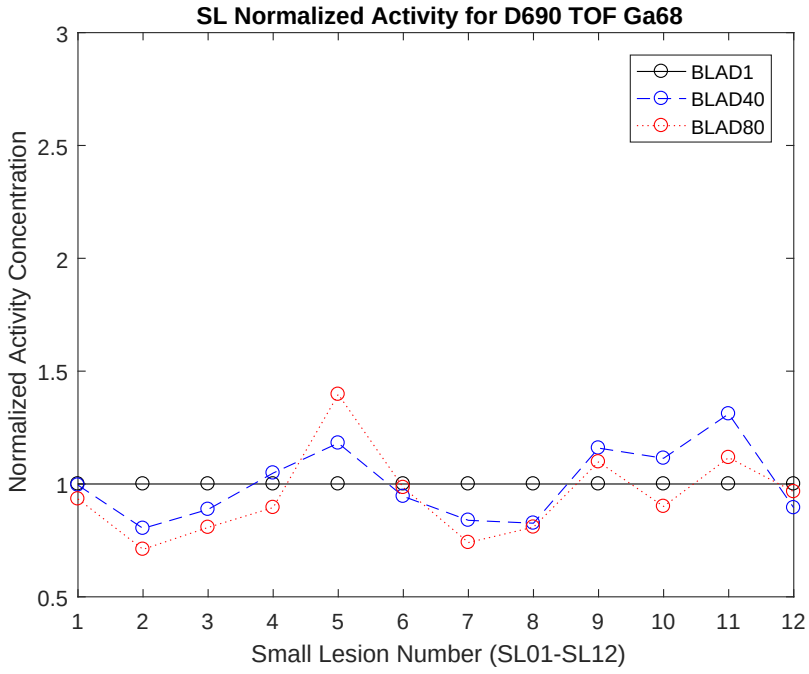

FIGURE 3.15: Normalized activity concentration to its corresponding BLAD1 scan for 12 SL with D690 TOF Ga68.

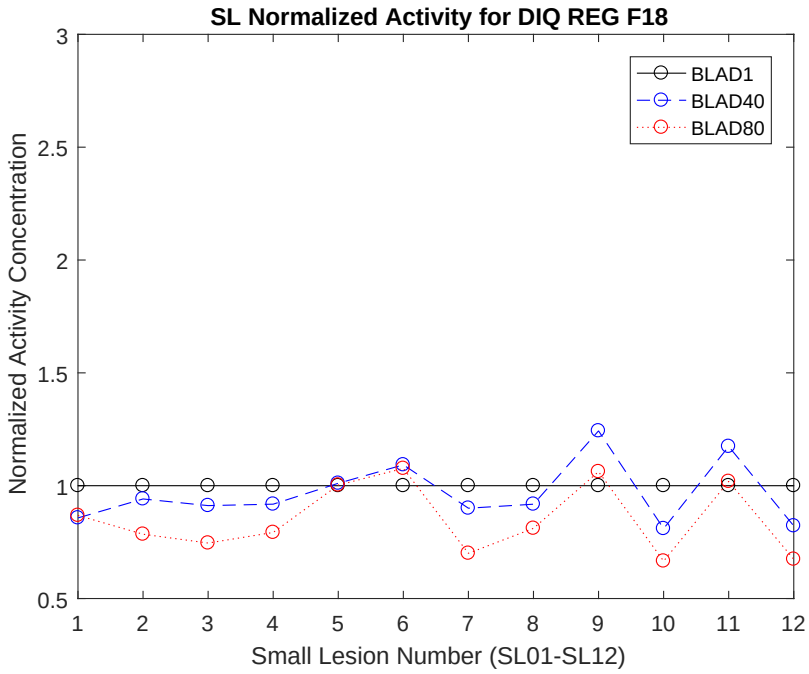

FIGURE 3.16: Normalized activity concentration to its corresponding BLAD1 scan for 12 SL with DIQ REG F18.

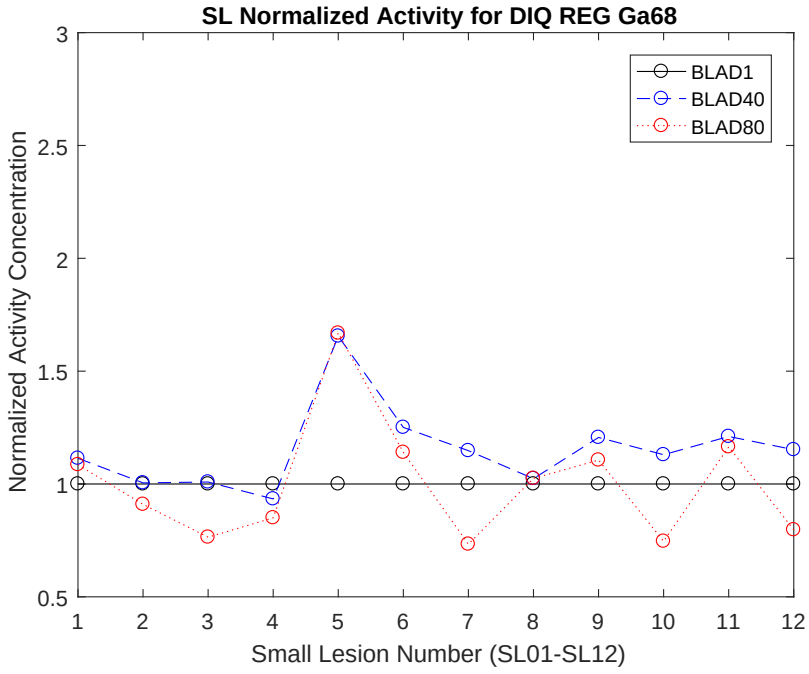

FIGURE 3.17: Normalized activity concentration to its corresponding BLAD1 scan for 12 SL with DIQ REG Ga68.

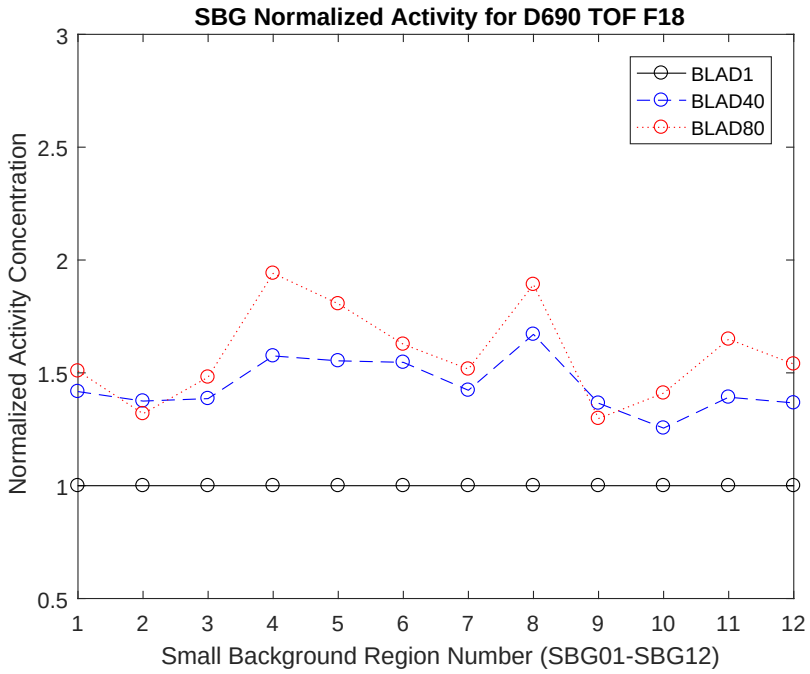

FIGURE 3.18: Normalized activity concentration to its corresponding BLAD1 scan for 12 SBG with D690 TOF F18.

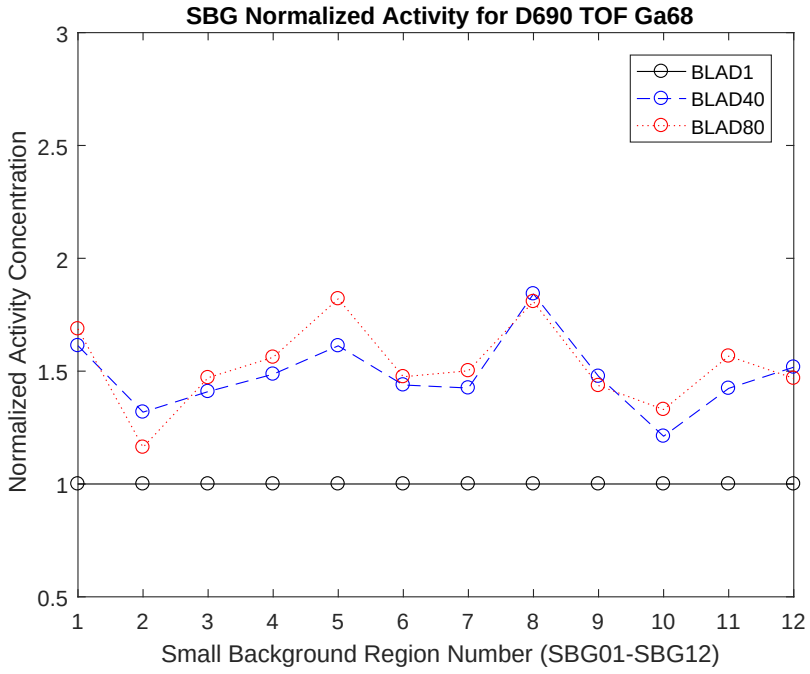

FIGURE 3.19: Normalized activity concentration to its corresponding BLAD1 scan for 12 SBG with D690 TOF Ga68.

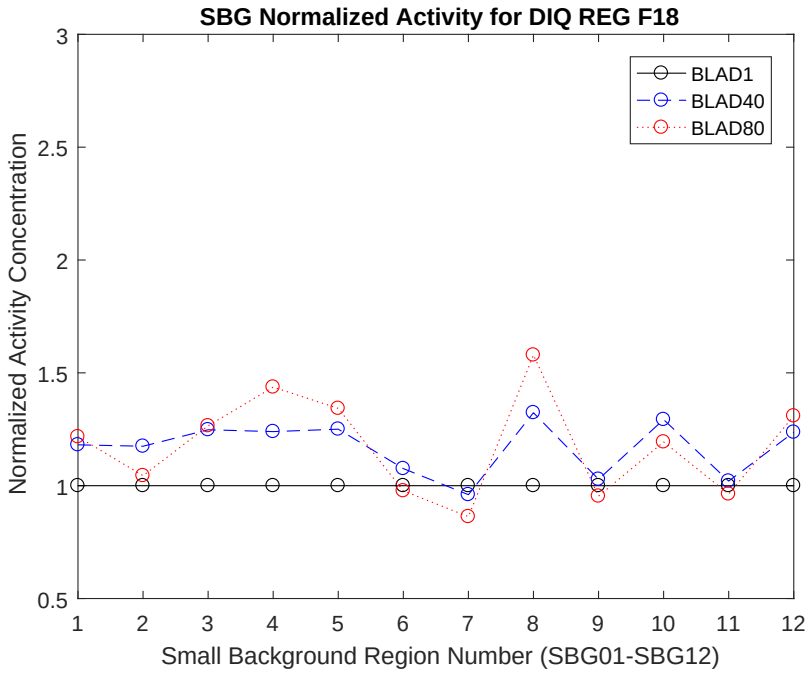

FIGURE 3.20: Normalized activity concentration to its corresponding BLAD1 scan for 12 SBG with DIQ REG F18.

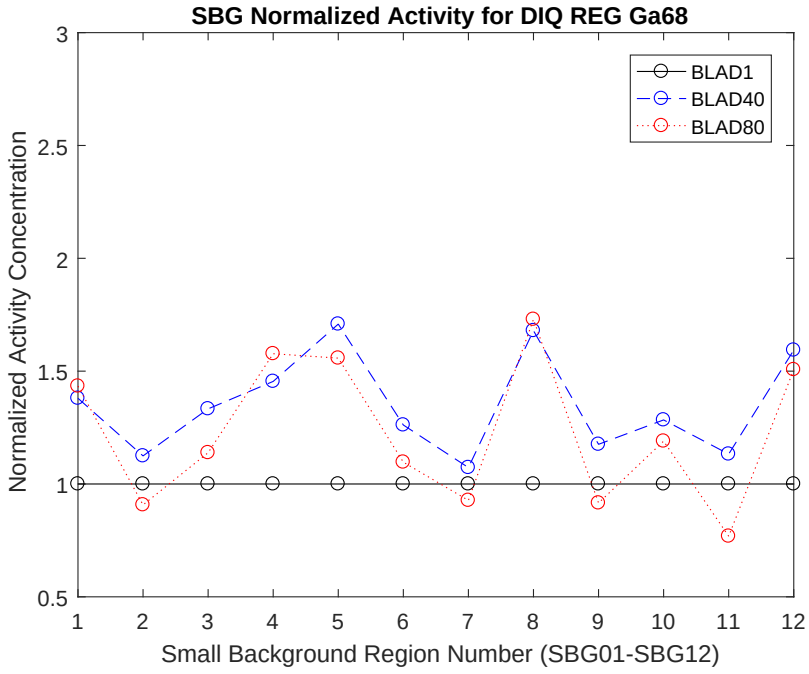

FIGURE 3.21: Normalized activity concentration to its corresponding BLAD1 scan for 12 SBG with DIQ REG Ga68.

(a) The Sum of Relative Activity Difference for 12 SL

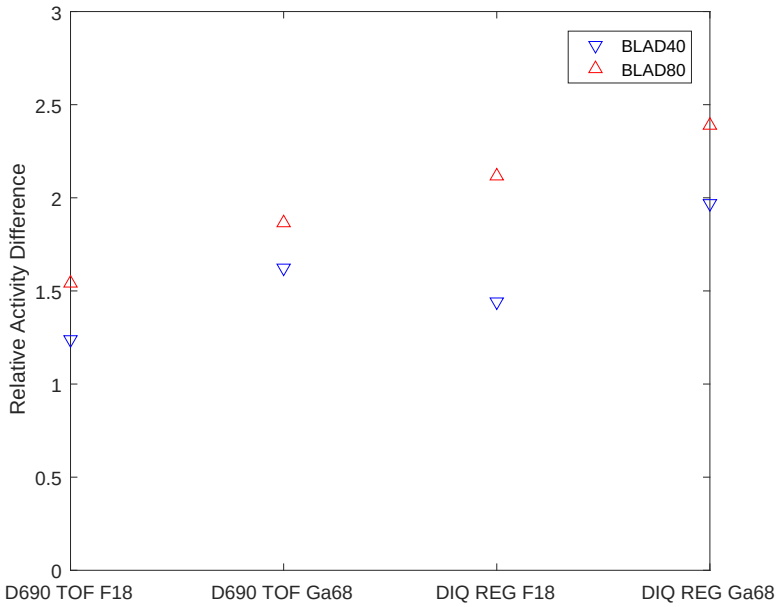

(b) The Sum of Relative Activity Difference for 12 SBG

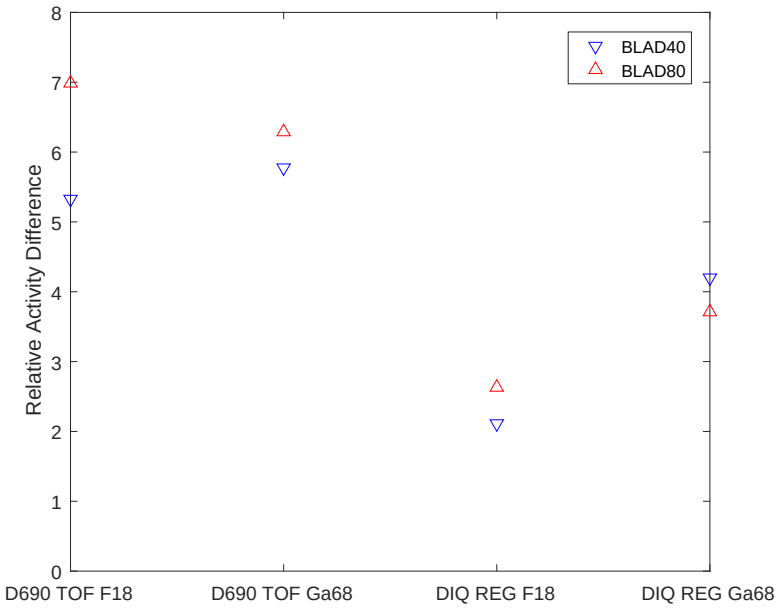

FIGURE 3.22: The sum of relative activity difference for BLAD40 and BLAD80 with different plans. (a) for 12 SL; (b) for 12 SBG.

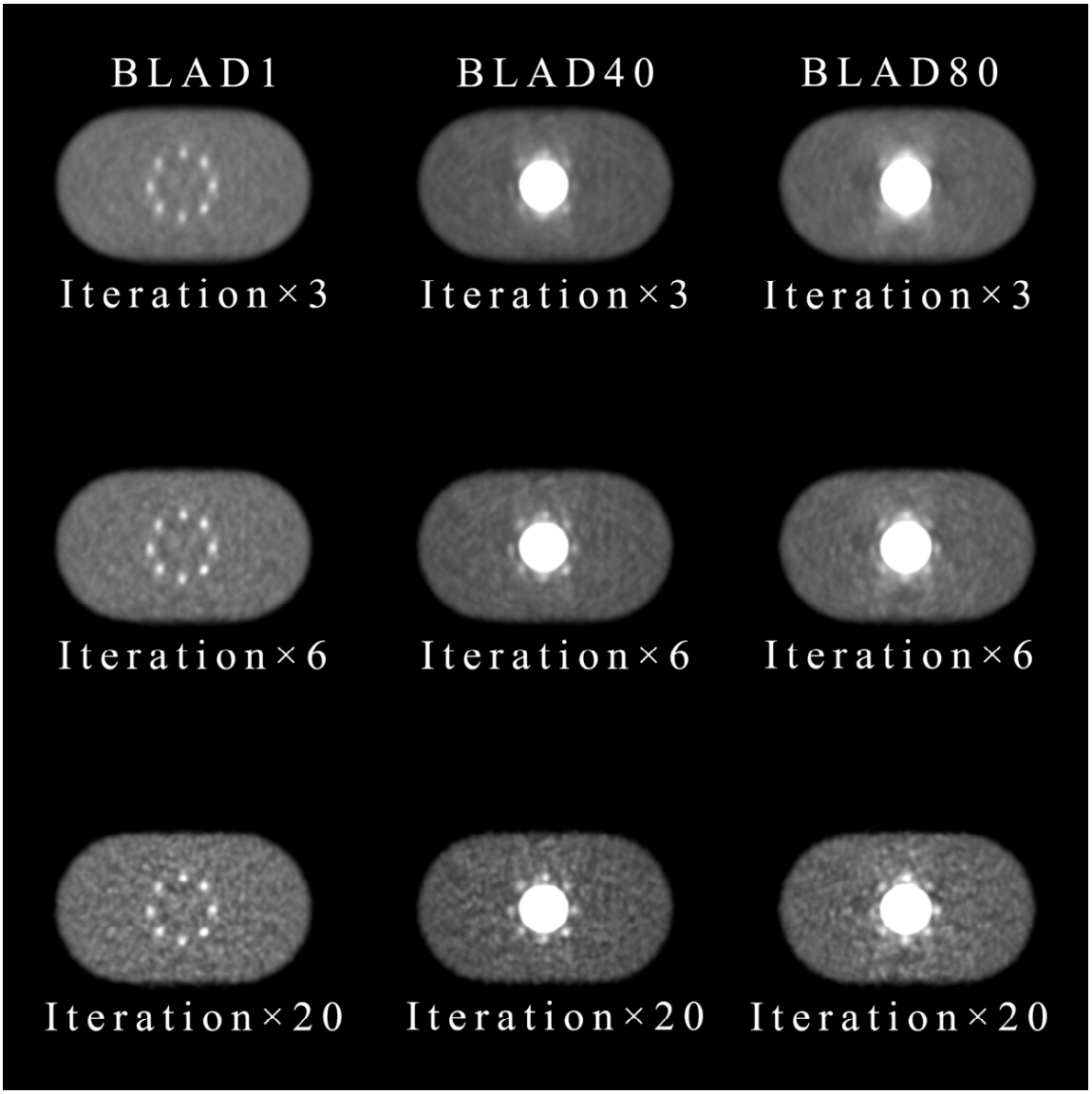

FIGURE 3.23: The effects of iteration number and bladder activity for D690 Ga68 nTOF. Each row represents the number of iterations, each column is one bladder concentration level. More iterations provided better lesion visualization, but also increased image noises.

Fig. 3.23 for D690 Ga68 nTOF demonstrates the effects of the number of iterations on lesions in the vicinity of the bladder. No matter what the bladder activity level was, more iterations made hot lesions more obvious, however, image noise sig-

nificantly increased.

Iteration Analyses for data reconstructed with varying iterations are applied to image sets under D690 Ga68 nTOF mode. Fig. 3.24 to 3.26 show the absolute value for each SL with iterations at three bladder concentration levels. The x-axis represents the number of lesions (SL01 - SL12) and the y-axis represents the absolute value. The next two figures compare the mean value of 12 SL to the background value. Fig. 3.27 shows SL-to-LBG ratio and Fig. 3.28 is the ratio of SL to the mean of 12 SBG. The x-axis represents the number of iterations and the y-axis represents the activity concentration ratio. Fig. 3.29 to Fig. 3.33 differ from the number of iterations. For each figure SL values at three bladder activity levels are normalized to the corresponding BLAD1 scan. The x-axis still represents the number of lesions (SL01 - SL12) and the y-axis represents normalized activity concentration. At last, Fig. 3.34 calculates the standard deviation (SD) for 12 SL in each image set, and the results are displayed with bladder concentration as x-axis and SD as y-axis.

Basically, more iterations increase SL values regardless of bladder radioactivity level. The only exception happens when one SL value is abnormally higher than others, such SL01 and SL05. The value gets lower in the beginning and then becomes higher. After 10 iterations, no significant change occurs on the SL values.

The ratio of SL to either LBG or SBG indicates similar effects. First, more iterations cause higher SL values, and thus providing better lesion contrast. Furthermore, the fact that the SL-to-SBG ratio is much lower than the SL-to-LBG ratio shows regions closer to the bladder are more affected. At last, the ratio of SL to the background is getting lower with higher bladder activity.

From Fig. 3.29 to Fig. 3.33 we can see that the value change due to artifact is getting smaller as the number of iterations increases. The artificially high-value point (e.g. SL05) gradually gets lower while the low-value point (e.g. SL07) becomes closer to its true value in BLAD1 scan. Overall, the difference in normalized activity

values among 12 SL is getting smaller as all SL values approach their true values. The decreased SD values with increased iterations in Fig. 3.34 also demonstrate the variability of 12 SL is getting smaller (best with 10 iterations). Besides, the effect that BLAD80 has more influence in the variation of SL values than BLAD40 is confirmed from this figure.

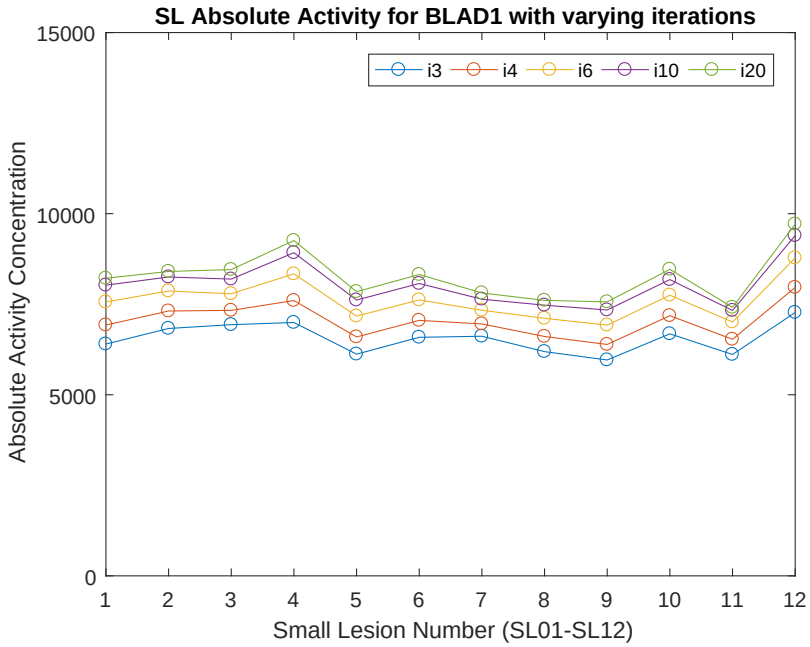

FIGURE 3.24: Absolute activity with varying iterations for every SL in BLAD1 D690 nTOF Ga68.

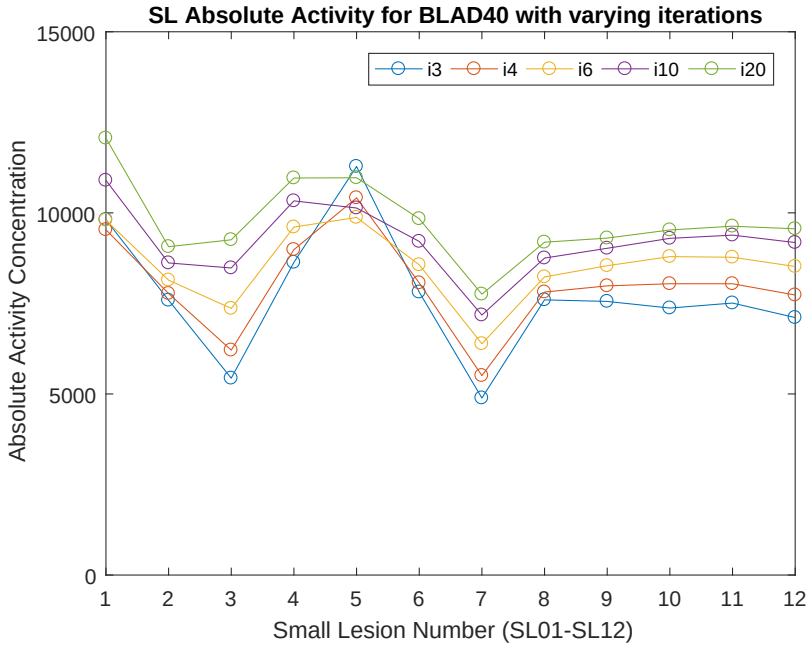

FIGURE 3.25: Absolute activity with varying iterations for every SL in BLAD40 D690 nTOF Ga68.

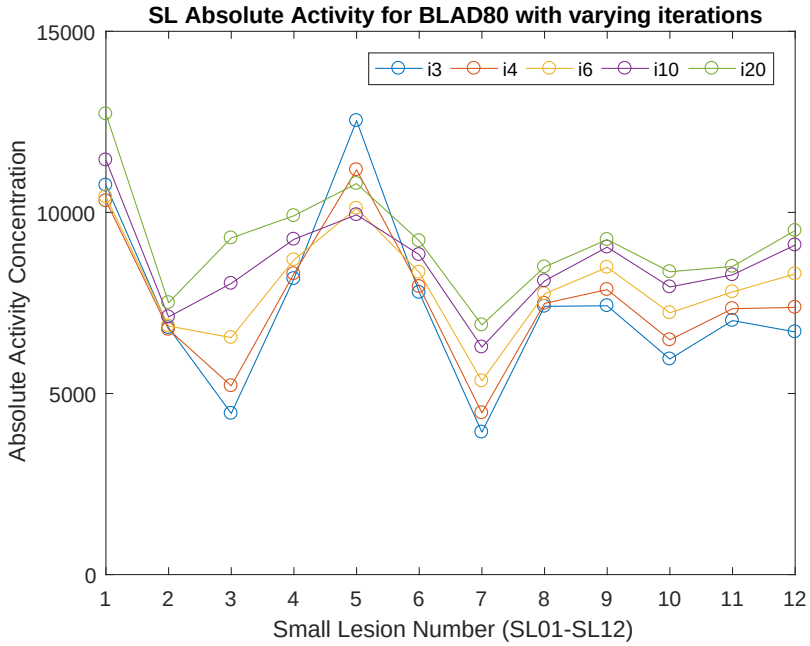

FIGURE 3.26: Absolute activity with varying iterations for every SL in BLAD80 D690 nTOF Ga68.

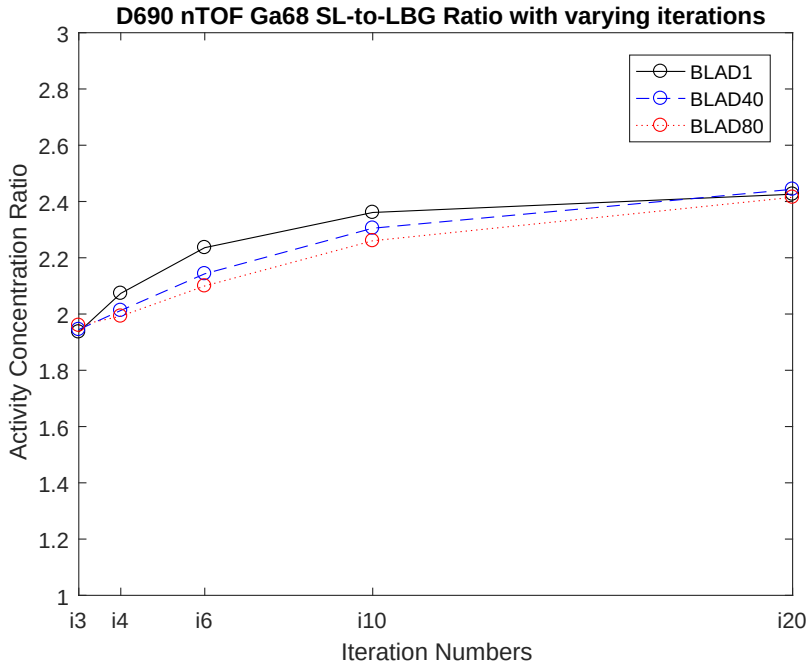

FIGURE 3.27: The ratio of the mean of 12 SL to LBG for varying bladder concentrations and iterations in image sets with D690 nTOF Ga68.

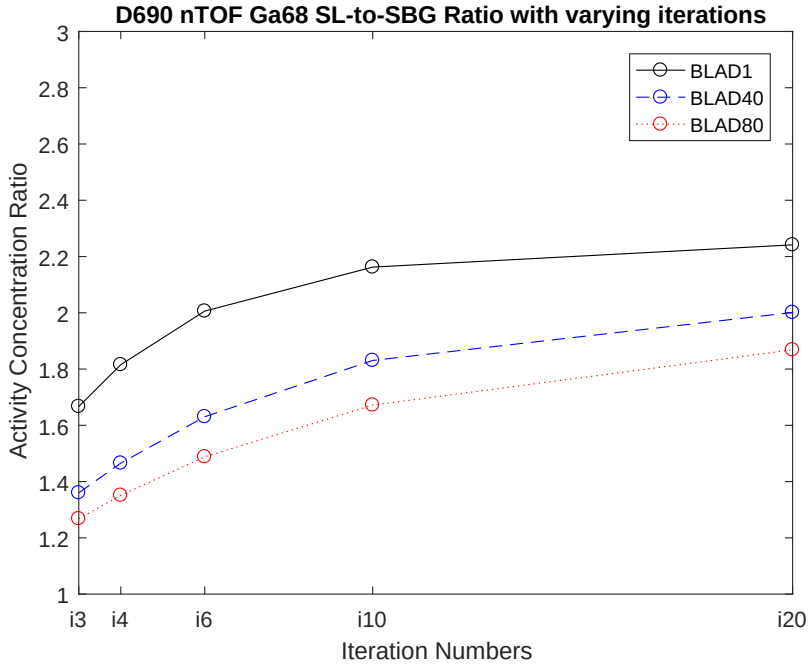

FIGURE 3.28: The ratio of the mean of 12 SL to the mean of 12 SBG for varying bladder concentrations and iterations in image sets with D690 nTOF Ga68.

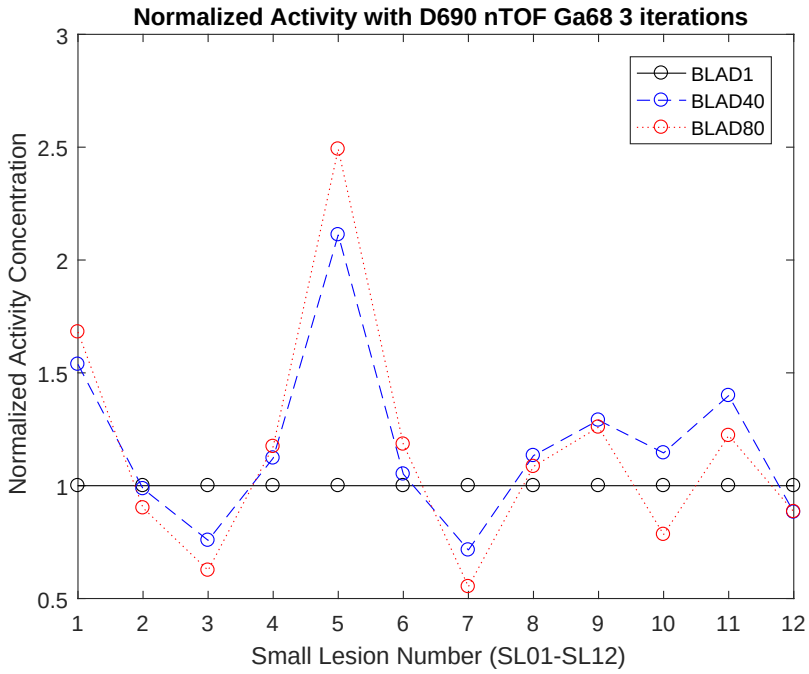

FIGURE 3.29: D690 nTOF Ga68 Normalized activity concentration to its corresponding BLAD1 scan for 12 SL with 3 iterations.

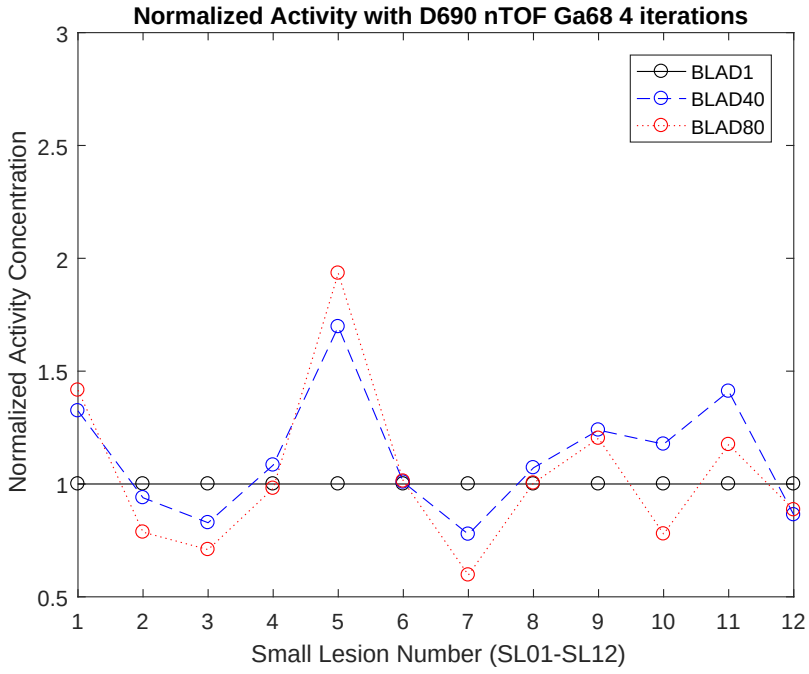

FIGURE 3.30: D690 nTOF Ga68 Normalized activity concentration to its corresponding BLAD1 scan for 12 SL with 4 iterations.

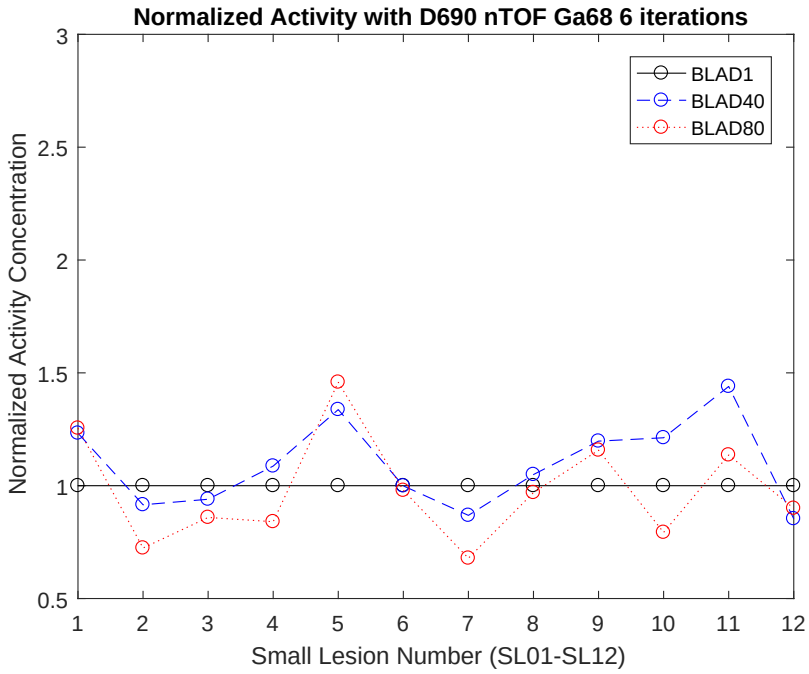

FIGURE 3.31: D690 nTOF Ga68 Normalized activity concentration to its corresponding BLAD1 scan for 12 SL with 6 iterations.

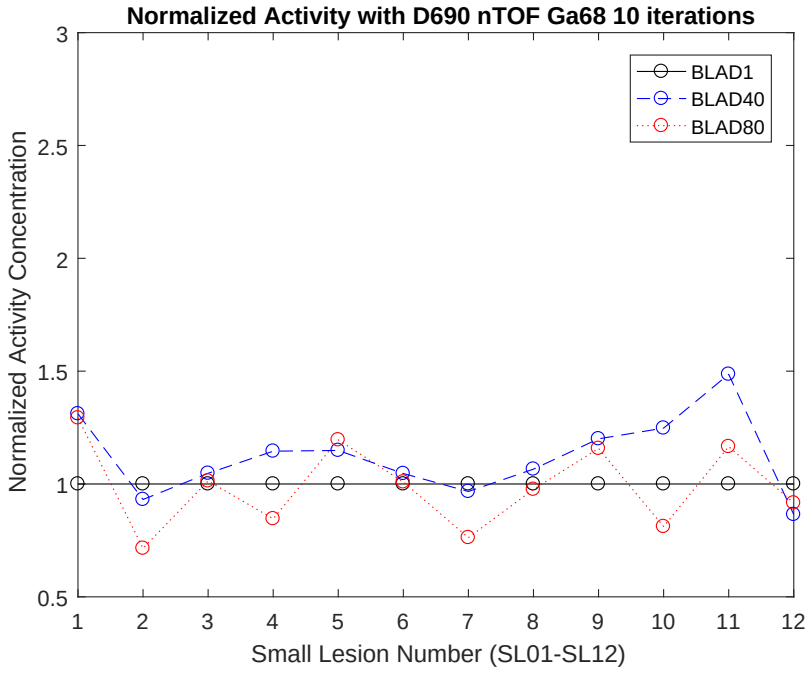

FIGURE 3.32: D690 nTOF Ga68 Normalized activity concentration to its corresponding BLAD1 scan for 12 SL with 10 iterations.

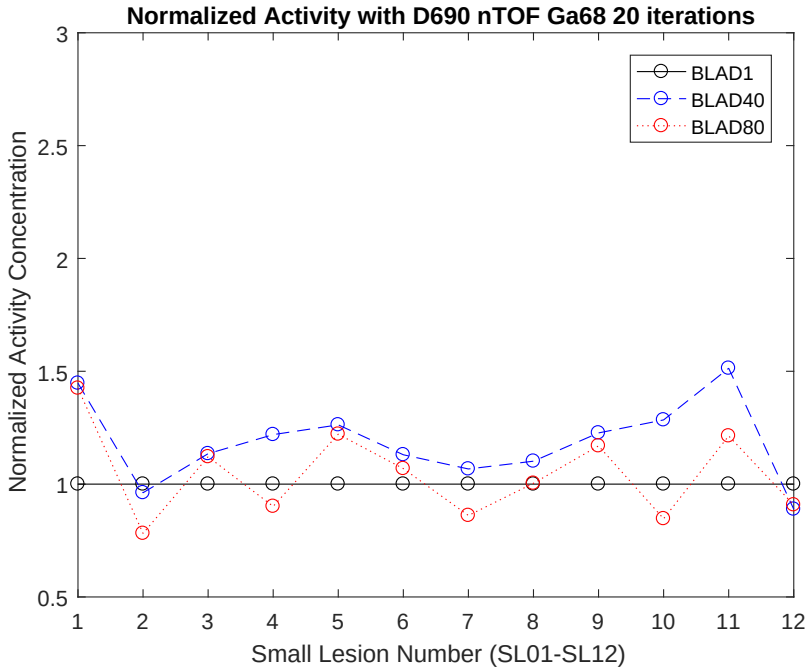

FIGURE 3.33: D690 nTOF Ga68 Normalized activity concentration to its corresponding BLAD1 scan for 12 SL with 20 iterations.

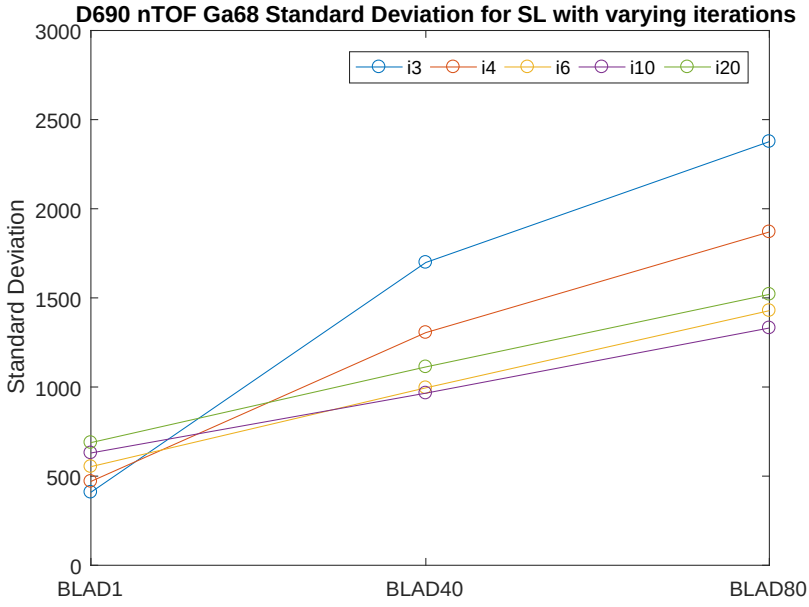

FIGURE 3.34: Standard Deviation for all SL with varying bladder concentrations and iterations under D690 nTOF Ga68 mode.

4

Discussion

The influence of bladder concentrations, the number of iterations and other factors in the vicinity of the bladder shown above is only from D690 Ga68 nTOF, but actually similar effects with negligible difference can be seen on data from the other machines and radionuclides. Four experimental groups were performed in four days, and all the ROI values are provided in the Appendix. As the signal-to-noise ratio (SNR) is proportional to the square root of the number of expected photons, the remaining activity during the beginning of PET scans may contribute slight effects to results when data from different groups were compared. We tried our best to keep the constancy of radioactivity during BLAD80 scan every day, and the same phantom filling protocol was followed as well in order to minimize this influence.

All the lesions around the bladder are more affected by BLAD80 activity level, however, there may be a question if we say this effect is more dramatic with increasing bladder activity. An exception of local minimum or local maximum may occur if value measurements do not increase monotonically with activity concentration. In the bladder concentration level study, we only consider bladder-to-background ratio of 1, 40 and 80. Currently speaking, we cannot exclude the possibility that local

minimum (maximum) occurs when the ratio is in the range of 1 to 40, or 40 to 80, although it is highly unlikely. In reality, the bladder activity level will not typically be as high as what we used in this study, and is usually lower than 40 [27]. More experimental groups with bladder ratio of 1 to 40 can be included in further studies.

Lesion value changes on the anteroposterior (e.g. SL01 and SL05) and lateral (e.g. SL03 and SL07) sides are opposite. This effect would not be observed with a phantom with circular, or near-circular cross section. If we take into consideration the other 4 small lesions in the edge-transverse plane, it is not accidental. Recall that (Fig. 2.5) SL01, SL05, SL09 and SL11 are in one mid-sagittal plane, and are lesions of which concentration values are the highest against their neighboring lesions. Meanwhile, SL03, SL07, SL10 and SL12 that have relative lower radioactivity concentrations are all in one mid-coronal plane. If the phantom and placement of 12 lesions are perfectly symmetrical, the effect of bladder activity in its vicinity should be the same. Thus, we may ascribe the opposite changes of lesion values to the dimensions of the oval phantom. The major axis (36 cm) along the lateral direction is much longer than the minor axis (21 cm) along the anteroposterior direction. The longer the reconstructed image is in one side, the lower values may occur in the vicinity of the bladder in that side. Another fact also links the value changes mentioned above to the phantom dimensions, or in other words, the relative position of lesions to the bladder. SL01, SL05, SL09 and SL11 have high activity values, however, values of SL01 and SL05 are relatively higher. In the mid-sagittal plane, SL01 and SL05 are in the mid-line while SL09 and SL11 are close to the edge of the bladder. To some degree we can say the more proportion of the bladder has in the anteroposterior direction, the more it affects to lesions existing along this direction, and it is the same with the lateral side. Other lesions (SS02, SS04, SS06 and SS08) located in between suffer from two opposite effects so that activity values do not vary a lot compared to control group.

Another factor that probably results in the opposite value changes in two directions is the existence of air bubbles on the top of bladder. The size of air bubbles may vary when the activity solution in the bladder is replaced. Attenuation correction error was thus the following consequence of distribution differences between CT and PET acquisitions [28]. Although we have tried our best during the phantom filling, there was still the possibility of attenuation mismatch. More efforts in phantom design or filling are required.

^{68}Ga has the property of emitting high-energy photons during its decay. 1077keV photons undergoing Compton scatter, and less likely pair-production, may attribute to worse image quality. It is possible for multi-scattered photons to be captured by detectors and accepted by ACD as coincidence events, which increases the total random events. As we know, an annihilation event does not exactly happen in the site where the positron was emitted. The distance error called effective positron range is determined mainly by the initial positron energy. Positrons emitted from ^{68}Ga have much higher energies than those from ^{18}F (836 keV vs. 250 keV, mean energy) [7], and thus spatial resolution is worse for images with ^{68}Ga than ^{18}F. Besides, the fact that the portion of positron emission is lower for ^{68}Ga than ^{18}F is also one factor that decreases the ratio of random-to-true coincidence counting rates. Therefore, using ^{68}Ga in PET scan may cause more loss of image contrast and distortion between lesion value and the actual amount of activity in that lesion.

However, ^{68}Ga PET images can be improved with either TOF technique or REG algorithm. It does not mean that without TOF information OSEM algorithm is not able to provide better bladder images. The results provided are based on the default settings adopted at DUMC, which are 2 (D690) and 4 (DIQ) iterations. In the real clinical case of reconstructing pelvic cavity, it is feasible to add more iterations (up to 6 or 10) to achieve equivalent image quality, and take into account the cost of time.

Partial decline of image quality will not hinder the more and more popular use of ^{68}Ga labeled compounds in detecting NETs, especially ^{68}Ga-DOTA compounds [29]. The oval phantom we use cannot simulate all clinical situations, and the abdomen size in clinic varies a lot from patient to patient. Some cancer patients receiving PET/CT exams may be plump at first, but usually become emaciated with the development of disease. Several authors have introduced some methods to improve pelvis imaging by using continuous irrigation and administration of diuretics [30,31]. Although great caution is still required in order to avoid misdiagnosis when assessing PET images [32, 33], true-positive detection rate can be significantly improved with further delayed images [34, 35]. These methods are sometimes limited because of more complex procedure, diuretic contraindication or urethral obstruction resulting from prostate cancer. Some scientists are now studying a new radionuclide Cooper-64 for PET/CT scan that will not accumulate in the bladder and they already have good results [36, 37]. Despite all the efforts, the artifact caused by high bladder radioactivity needs more attention before ^{64}Cu is widely adopted in clinic.

5

Conclusions

It was proved that ^{68}Ga and ^{18}F bladder radioactivity concentrations have serious effects on the value variations in the vicinity of the bladder, which agrees with previous studies on SUV analysis of ^{18}F-FDG PET imaging. Comparison studies demonstrate the relationships between value variations and other factors, and are also provided as followed:

1. Higher bladder-to-background radioactivity ratio has more dramatic effects on lesion measurements close to the bladder, and value changes in the anteroposterior and lateral directions are totally opposite.

2. ^{68}Ga accumulated in the bladder brings about greater variations in lesion values than ^{18}F.

3. Bayesian penalized likelihood reconstruction algorithm or OSEM algorithm with TOF information can significantly lower the variability in lesion activity measurements. If TOF information is not available, OSEM alone with more iterations is also able to provide improved image quality.

Appendix A

Data of ROI Values

The following data are measurements of four ROIs from four acquisitions: D690F18, D690Ga68, DIQF18 and DIQGa68. Decay correction was applied to them according to the time when BLAD80 scan was performed.

Table A.1: Max Values of SL for D690 F18

max		SL01	SL02	SL03	SL04	SL05	SL06	SL07	SL08	SL09	SL10	SL11	SL12
	Default	5196	6706	6295	6803	7087	7253	7352	6759	6763	7362	7233	7772
	3 iterations	5382	6953	6422	7078	7411	7596	7848	7225	7001	7516	7873	8407
	4 iterations	5963	7704	6866	7870	8351	8514	8639	8080	7834	8318	8938	9448
nTOF	6 iterations	6735	8572	7368	8828	9435	9614	9591	9132	8817	9270	10129	10594
BLAD1	10 iterations	7405	9185	7727	9594	10240	10468	10411	9955	9530	10056	10930	11375
	20 iterations	7790	9451	7806	10057	10674	10990	10899	10352	9897	10551	11313	11721
	4mm	5872	7793	7123	7949	8581	8860	8738	8142	7739	8696	8716	9550
	Default	8485	7559	4941	6969	9981	7490	5695	8350	8765	7526	7123	7858
	3 iterations	8376	7755	5569	7230	9649	7736	6223	8950	9204	7824	7303	8425
	4 iterations	8211	8374	6681	7732	8878	8411	7446	10134	10455	8807	8197	9531
nTOF	6 iterations	8945	9610	8184	8638	9235	9416	8999	11857	11995	9898	9489	10932
BLAD40	10 iterations	10889	11076	9484	9908	10831	10323	10323	13477	13130	10661	10568	12193
	20 iterations	12858	12321	10510	11322	12502	10722	11312	14595	13656	11093	11090	13204
	4mm	8948	8449	5563	7576	10328	8181	6468	9545	10482	8696	8182	9304
	Default	9440	6272	4542	8168	12405	7984	4300	7335	7432	6814	7239	7391
	3 iterations	9090	6365	5082	7852	11467	7927	4640	7396	7710	7347	7322	7880
	4 iterations	8298	6651	6410	8330	10003	8533	5701	7798	8689	8471	8076	8956
nTOF	6 iterations	8265	7318	8405	9263	8882	9721	7280	8596	9981	9964	9317	10377
BLAD80	10 iterations	9456	8084	10062	10541	9775	11128	8614	9635	10994	11244	10449	11628
	20 iterations	11532	8636	10995	12114	12082	12203	9391	10855	11401	11990	11145	12442
	4mm	9859	6380	4709	8478	12095	9109	4768	7708	8450	7750	8018	8702
	Default	7290	8045	8240	8392	8992	8878	8949	9153	9248	9120	8988	9075
	3 iterations	7621	8068	8470	8343	9271	9001	9517	9945	9184	8912	9660	9298
	4 iterations	8088	8528	9005	8864	9857	9528	10196	10634	9780	9484	10350	9868
TOF	6 iterations	8452	8879	9427	9323	10355	9949	10746	11167	10218	9948	10907	10334
BLAD1	10 iterations	8627	9027	9594	9602	10656	10163	11008	11451	10413	10206	11224	10594
	20 iterations	8651	9025	9608	9697	10762	10205	11073	11576	10446	10305	11362	10681
	4mm	8590	9909	10166	10269	11764	11075	11201	11824	11678	11380	11444	11023
	Default	6138	7886	6479	6775	7286	7913	7983	9711	10084	9854	8987	9224
	3 iterations	6414	7890	7020	7104	7389	8363	8501	10431	10404	10051	9157	9980
	4 iterations	6924	8709	7808	7667	8079	9122	9479	11761	11266	11013	9917	10907
TOF	6 iterations	8055	9810	8641	8537	9676	10025	10486	13219	11975	11869	10637	11765
BLAD40	10 iterations	9326	10735	9423	9474	11245	10678	11261	14238	12390	12391	11114	12297
	20 iterations	9787	11242	9986	10148	11589	11023	11918	14890	12572	12646	11354	12609
	4mm	6827	9281	7338	7743	8363	8859	9552	12253	12690	12253	10796	11031
	Default	6226	6277	6637	7208	8325	7593	7099	6605	8816	9026	8480	9281
	3 iterations	6380	6930	7972	7479	7869	7703	7633	7256	9132	9602	8640	9891
	4 iterations	6776	7512	9233	8017	7742	8299	8600	7857	9987	10713	9451	10989
TOF	6 iterations	8029	8356	10550	8921	8748	9267	9543	8703	10828	11822	10286	12073
BLAD80	10 iterations	10000	9184	11434	9910	10810	10174	10187	9621	11301	12510	10798	12781
	20 iterations	11201	9734	12044	10622	12153	10854	10718	10525	11489	12791	11023	13195
	4mm	6881	6782	7730	8260	8174	8817	8194	7073	10572	10848	9808	11626

Table A.2: Mean Values of SL for D690 F18

mean		SL01	SL02	SL03	SL04	SL05	SL06	SL07	SL08	SL09	SL10	SL11	SL12
	Default	3926	4756	4531	4699	4910	4990	5042	4728	5159	5272	5122	5271
	3 iterations	3983	4817	4593	4790	5071	5130	5272	4935	5247	5333	5439	5469
	4 iterations	4226	5124	4768	5084	5463	5477	5567	5258	5678	5665	5908	5843
nTOF	6 iterations	4542	5485	4981	5428	5894	5867	5915	5625	6171	6028	6416	6222
BLAD1	10 iterations	4825	5762	5174	5702	6200	6149	6200	5869	6515	6292	6749	6459
	20 iterations	5007	5901	5278	5879	6345	6292	6367	5966	6676	6415	6882	6535
	4mm	4105	5041	4715	4937	5238	5299	5353	5001	5517	5612	5467	5587
	Default	6602	5340	3774	5437	7691	5816	3874	6243	6319	5472	5693	5316
	3 iterations	6476	5436	4072	5529	7391	5918	4107	6507	6535	5616	5756	5542
	4 iterations	6131	5622	4640	5617	6823	6119	4636	6931	7051	6077	6116	5951
nTOF	6 iterations	6084	5981	5424	5800	6525	6445	5312	7523	7647	6591	6596	6409
BLAD40	10 iterations	6561	6427	6138	6042	6797	6734	5865	8049	8024	6970	6990	6737
	20 iterations	7141	6819	6652	6320	7369	6845	6237	8396	8133	7178	7187	6929
	4mm	6718	5486	3841	5537	7776	5909	4009	6489	6769	5829	5955	5612
	Default	7461	5122	3356	6136	8991	5958	3314	5459	6026	5196	5861	5322
	3 iterations	7254	5276	3697	6284	8583	6046	3540	5686	6147	5443	5921	5555
	4 iterations	6656	5326	4330	6426	7677	6237	4127	5855	6542	5987	6229	6025
nTOF	6 iterations	6325	5500	5306	6734	7044	6623	5011	6156	7058	6693	6662	6588
BLAD80	10 iterations	6594	5728	6208	7152	7128	7063	5796	6496	7475	7318	7060	7012
	20 iterations	7377	5889	6823	7657	7906	7397	6234	6811	7703	7718	7309	7227
	4mm	7565	5189	3317	6246	8956	6049	3399	5546	6344	5456	6109	5580
	Default	4780	5087	5212	5266	5625	5706	5552	5564	6166	5770	5845	5541
	3 iterations	4870	5018	5316	5169	5743	5773	5780	5810	6110	5669	6166	5699
	4 iterations	5085	5197	5562	5379	5965	5991	6049	6049	6400	5920	6457	5932
TOF	6 iterations	5273	5340	5778	5560	6152	6161	6267	6235	6617	6114	6691	6114
BLAD1	10 iterations	5377	5403	5901	5661	6264	6241	6368	6334	6717	6199	6818	6206
	20 iterations	5391	5408	5955	5695	6306	6258	6375	6366	6745	6201	6844	6226
	4mm	5167	5520	5637	5694	6189	6214	6049	6088	6834	6332	6395	6073
	Default	4617	5391	4758	5015	5636	5672	5171	6137	7000	6271	6558	5886
	3 iterations	4721	5407	4964	5122	5642	5786	5406	6427	7219	6349	6495	6156
	4 iterations	4831	5678	5332	5270	5698	6006	5813	6809	7597	6742	6819	6521
TOF	6 iterations	5226	6040	5722	5521	6093	6300	6229	7211	7894	7084	7132	6848
BLAD40	10 iterations	5734	6340	6003	5805	6580	6561	6535	7476	8016	7274	7330	7036
	20 iterations	5953	6495	6142	6014	6755	6749	6743	7610	8009	7348	7423	7116
	4mm	4776	5635	4898	5197	5829	5843	5460	6483	7703	6860	7038	6362
	Default	4797	5042	4664	5611	5999	5782	4964	5250	6455	6163	6543	6140
	3 iterations	4805	5343	5194	5755	5881	5852	5326	5597	6561	6404	6554	6389
	4 iterations	4783	5536	5697	5946	5668	6022	5810	5826	6895	6890	6857	6809
TOF	6 iterations	5099	5850	6234	6306	5836	6312	6306	6165	7227	7387	7171	7204
BLAD80	10 iterations	5728	6159	6612	6742	6412	6618	6654	6509	7426	7716	7364	7426
	20 iterations	6126	6339	6860	7125	6784	6887	6929	6740	7513	7873	7432	7515
	4mm	4935	5204	4714	5776	6043	5936	5183	5405	6903	6584	6943	6590

Table A.3: Mean Values of SBG for D690 F18

mean		SBG01	SBG02	SBG03	SBG04	SBG05	SBG06	SBG07	SBG08	SBG09	SBG10	SBG11	SBG12
	Default	2977	3211	3395	2479	2673	3442	3394	2660	3131	3372	2784	2932
	3 iterations	2956	3172	3340	2433	2654	3410	3354	2704	3065	3324	2786	2860
	4 iterations	2966	3072	3263	2360	2622	3306	3267	2690	3026	3313	2697	2790
nTOF	6 iterations	3002	2920	3141	2276	2596	3131	3144	2697	2975	3288	2574	2695
BLAD1	10 iterations	3074	2765	3017	2209	2582	2940	3039	2735	2938	3265	2446	2585
	20 iterations	3129	2671	2938	2182	2546	2800	2990	2772	2926	3275	2362	2453
	4mm	2972	3178	3376	2415	2647	3422	3379	2638	3165	3375	2737	2882
	Default	5479	3250	3695	5324	5966	4096	3558	5950	3842	3760	3459	3715
	3 iterations	5213	3227	3698	5124	5699	4033	3521	5665	3850	3773	3421	3768
	4 iterations	4801	3321	3833	4694	5197	4154	3637	5247	3931	3835	3373	3770
nTOF	6 iterations	4397	3351	3924	4257	4745	4239	3712	4887	4050	3934	3307	3784
BLAD40	10 iterations	4092	3218	3878	3890	4485	4199	3693	4705	4188	4095	3246	3825
	20 iterations	3939	2970	3737	3597	4465	4061	3646	4692	4249	4290	3242	3894
	4mm	5427	3200	3695	5210	5893	4086	3503	5886	3911	3826	3437	3684
	Default	6159	2901	3697	6616	6936	3854	3240	7114	3508	3877	3737	3947
	3 iterations	5774	2910	3697	6373	6570	3833	3250	6767	3487	3892	3763	3950
	4 iterations	5226	3024	3861	5858	5882	3986	3450	6235	3475	3929	3763	3939
nTOF	6 iterations	4696	3121	3967	5358	5243	4105	3682	5789	3445	3946	3763	3918
BLAD80	10 iterations	4316	3051	3841	4956	4823	3999	3787	5554	3404	3942	3787	3889
	20 iterations	4183	2775	3517	4662	4699	3669	3788	5478	3370	3977	3881	3822
	4mm	6057	2813	3639	6509	6806	3815	3214	7026	3488	3886	3739	3956
	Default	2858	2672	2839	2296	2590	2737	2747	2307	2660	2739	2443	2497
	3 iterations	2823	2698	2771	2270	2582	2656	2697	2350	2579	2670	2446	2394
	4 iterations	2857	2623	2696	2224	2584	2532	2629	2348	2583	2665	2415	2368
TOF	6 iterations	2906	2554	2619	2178	2590	2388	2573	2362	2614	2677	2398	2342
BLAD1	10 iterations	2938	2524	2577	2146	2581	2279	2557	2375	2664	2711	2412	2314
	20 iterations	2932	2524	2579	2136	2552	2246	2571	2365	2692	2754	2465	2300
	4mm	2857	2638	2822	2229	2569	2660	2709	2285	2695	2744	2415	2460
	Default	4051	3674	3935	3616	4023	4233	3909	3855	3632	3437	3401	3412
	3 iterations	3857	3519	3826	3500	3886	4061	3775	3694	3612	3409	3355	3510
	4 iterations	3677	3491	3815	3290	3648	3990	3756	3507	3652	3436	3340	3516
TOF	6 iterations	3514	3399	3749	3089	3458	3845	3694	3378	3722	3512	3350	3552
BLAD40	10 iterations	3423	3279	3639	2941	3374	3642	3630	3373	3800	3634	3398	3619
	20 iterations	3435	3227	3536	2900	3402	3429	3633	3474	3838	3737	3469	3698
	4mm	4003	3622	3944	3528	3943	4199	3857	3804	3721	3497	3408	3414
	Default	4311	3524	4205	4457	4678	4452	4167	4364	3452	3862	4029	3843
	3 iterations	4183	3526	4115	4290	4439	4338	4173	4187	3413	3818	4078	3826
	4 iterations	3937	3519	4083	4046	4103	4285	4268	3920	3364	3804	4099	3791
TOF	6 iterations	3725	3447	3959	3841	3837	4124	4315	3700	3313	3791	4153	3761
BLAD80	10 iterations	3610	3319	3771	3710	3717	3858	4294	3570	3284	3797	4249	3754
	20 iterations	3656	3211	3614	3689	3771	3554	4301	3544	3265	3821	4365	3777
	4mm	4231	3432	4166	4379	4582	4404	4171	4298	3427	3876	4082	3836

Table A.4: Mean Values of LBG & BLADDER for D690 F18

mean		LBG	BLADDER	mean		LBG	BLADDER
	Default	2709	2798		Default	2671	2303
	3 iterations	2711	2818		3 iterations	2673	2351
	4 iterations	2718	2805		4 iterations	2673	2368
nTOF	6 iterations	2724	2797	TOF	6 iterations	2672	2393
BLAD1	10 iterations	2727	2801	BLAD1	10 iterations	2672	2410
	20 iterations	2727	2802		20 iterations	2672	2411
	4mm	2711	2795		4mm	2673	2299
	Default	3013	103612		Default	2912	104201
	3 iterations	3020	104102		3 iterations	2919	104580
	4 iterations	3026	104331		4 iterations	2921	104579
nTOF	6 iterations	3032	104513	TOF	6 iterations	2923	104592
BLAD40	10 iterations	3036	104622	BLAD40	10 iterations	2923	104611
	20 iterations	3037	104657		20 iterations	2924	104611
	4mm	3014	103930		4mm	2913	104508
	Default	2977	199584		Default	2835	199405
	3 iterations	2984	199975		3 iterations	2844	199428
	4 iterations	2991	200318		4 iterations	2848	199462
nTOF	6 iterations	2997	200639	TOF	6 iterations	2851	199517
BLAD80	10 iterations	3000	200863	BLAD80	10 iterations	2852	199565
	20 iterations	3001	200954		20 iterations	2853	199579
	4mm	2978	200284		4mm	2836	200153

Table A.5: Max Values of SL for D690 Ga68

max		SL01	SL02	SL03	SL04	SL05	SL06	SL07	SL08	SL09	SL10	SL11	SL12
	Default	7655	8655	8293	9243	7576	8306	8393	7690	7290	8430	7010	9500
	3 iterations	8140	9123	8787	9690	7875	8638	8536	7913	7620	8884	7147	10198
	4 iterations	9154	10151	9517	11006	8837	9588	9199	8800	8543	9929	7839	11697
nTOF	6 iterations	10493	11394	10393	12650	10071	10750	9931	9944	9766	11161	8816	13559
BLAD1	10 iterations	11595	12364	11188	13995	11059	11646	10470	10860	10730	12081	9648	15045
	20 iterations	12204	12972	11771	14878	11517	12091	10749	11293	11140	12688	10043	15964
	4mm	9002	10010	9447	10834	8624	9592	9469	8899	8554	9949	7724	12034
	Default	12756	8659	6312	10787	17176	9032	5930	8663	9674	9248	9628	8477
	3 iterations	12518	9000	6658	10875	16630	9082	6102	8968	9831	10174	10001	9001
	4 iterations	12121	9532	7883	11928	14996	9666	7150	9431	10584	11681	11060	10100
nTOF	6 iterations	12935	10430	9768	13750	13467	10741	8625	10435	11695	13531	12693	11574
BLAD40	10 iterations	15201	11514	11718	16029	12703	12185	10122	11574	12878	15072	14339	13009
	20 iterations	17662	12478	13359	18142	14541	13664	11471	12441	13667	16298	15199	14191
	4mm	13615	9154	7005	12266	16717	9573	6670	9038	10755	10787	10952	9342
	Default	13949	8497	5181	11566	20781	10386	4735	8665	9377	6794	8468	8510
	3 iterations	13686	8224	5494	11371	19620	10226	4717	8585	9595	6963	8735	9025
	4 iterations	12959	7984	6748	10792	17091	9709	5488	8834	10272	7729	9207	10357
nTOF	6 iterations	13167	8247	8931	10631	14690	10526	6741	9640	11304	8852	10015	12199
BLAD80	10 iterations	14991	8841	11338	11839	13221	11750	7982	10602	12419	9802	11246	13778
	20 iterations	17392	10140	13198	13411	14064	12923	9255	11336	13027	10743	12188	14495
	4mm	14640	8508	5753	10746	19787	9510	5122	8695	10351	7309	9387	9538
	Default	9556	11035	9708	10420	10320	9139	9752	10150	9608	9984	8718	10611
	3 iterations	10049	11308	10207	10665	10644	9568	10000	10102	9420	10237	8754	11388
	4 iterations	10696	12104	10871	11379	11288	10136	10603	10806	10023	11001	9324	12259
TOF	6 iterations	11244	12763	11460	11989	11812	10586	11104	11385	10463	11668	9785	12980
BLAD1	10 iterations	11561	13126	11790	12350	12098	10776	11364	11688	10636	12074	9995	13380
	20 iterations	11665	13257	11920	12502	12213	10790	11457	11807	10601	12233	10074	13569
	4mm	11478	13730	11488	12518	12597	10784	11606	12497	11818	12128	10111	13738
	Default	9507	8863	8613	10925	12190	8636	8182	8386	11135	11122	11426	9491
	3 iterations	9771	9393	8984	11081	11803	9003	8520	8810	11118	12270	11563	10128
	4 iterations	10627	10114	10026	12333	10974	9615	9490	9541	11997	13374	12620	11063
TOF	6 iterations	12415	11081	11239	14110	10651	10558	10572	10581	12935	14352	13730	12019
BLAD40	10 iterations	14364	11949	12236	15751	12199	11602	11412	11574	13510	14910	14318	12654
	20 iterations	15108	12474	13005	16872	13042	12442	12063	12266	13681	15115	14467	12956
	4mm	11042	9767	9653	13399	11554	9492	9554	9378	12745	13083	13604	11001
	Default	8922	7839	7839	9332	14419	8995	7221	8208	10548	8990	9738	10248
	3 iterations	8835	8256	8240	9318	13712	8795	7202	8546	10750	9296	10163	11057
	4 iterations	9219	8755	9448	9980	12407	8892	8110	9239	11694	10303	11067	12399
TOF	6 iterations	10770	9688	10957	11143	11685	9526	9162	10286	12822	11399	12027	13822
BLAD80	10 iterations	13016	10822	12257	12614	14130	10287	9947	11333	13541	12105	12591	14700
	20 iterations	14308	12057	13432	13887	16062	11078	10429	12028	13629	12323	12790	15042
	4mm	9352	8463	8914	9955	13532	8495	8085	8955	12133	10288	11313	12633

Table A.6: Mean Values of SL for D690 Ga68

mean		SL01	SL02	SL03	SL04	SL05	SL06	SL07	SL08	SL09	SL10	SL11	SL12
	Default	6138	6597	6643	6758	5981	6446	6507	6128	5841	6453	6011	6925
	3 iterations	6400	6831	6935	6995	6121	6586	6616	6191	5961	6682	6112	7272
	4 iterations	6925	7313	7330	7601	6596	7054	6956	6609	6389	7183	6531	7963
nTOF	6 iterations	7561	7865	7789	8338	7172	7618	7334	7111	6922	7749	7009	8779
BLAD1	10 iterations	8026	8251	8194	8922	7615	8072	7639	7473	7340	8180	7327	9395
	20 iterations	8218	8405	8456	9259	7847	8320	7811	7606	7565	8463	7413	9710
	4mm	6539	6994	7035	7289	6293	6815	6851	6476	6181	6861	6284	7510
	Default	9914	7423	5161	8553	11601	7640	4644	7413	7413	6915	7310	6865
	3 iterations	9813	7588	5435	8633	11280	7812	4888	7598	7555	7372	7510	7109
	4 iterations	9534	7772	6210	8985	10415	8066	5507	7813	7984	8043	8042	7731
nTOF	6 iterations	9796	8142	7361	9607	9874	8565	6386	8231	8541	8792	8775	8519
BLAD40	10 iterations	10898	8617	8478	10331	10134	9211	7179	8752	9022	9296	9385	9180
	20 iterations	12063	9066	9257	10962	10969	9837	7754	9190	9304	9528	9631	9560
	4mm	10219	7639	5322	8844	11583	7786	4766	7565	7769	7309	7749	7241
	Default	10936	6695	4183	8082	13091	7505	3803	7203	7251	5799	6870	6468
	3 iterations	10751	6816	4450	8169	12534	7791	3932	7406	7422	5951	7014	6701
	4 iterations	10318	6769	5212	8305	11176	7952	4466	7489	7869	6480	7341	7377
nTOF	6 iterations	10431	6862	6544	8689	10113	8346	5347	7750	8483	7227	7806	8301
BLAD80	10 iterations	11446	7115	8039	9258	9935	8834	6281	8109	9041	7941	8277	9098
	20 iterations	12720	7508	9294	9908	10796	9216	6893	8494	9249	8362	8509	9499
	4mm	11107	6770	4258	8175	12941	7504	3834	7301	7573	6019	7089	6875
	Default	7274	7547	7023	7252	7184	6660	6830	7144	6899	6929	6713	7362
	3 iterations	7558	7642	7254	7408	7367	6828	6974	7114	6864	6990	6826	7696
	4 iterations	7885	8004	7591	7754	7675	7109	7280	7455	7198	7345	7143	8101
TOF	6 iterations	8135	8300	7892	8052	7930	7352	7554	7735	7456	7647	7396	8423
BLAD1	10 iterations	8246	8454	8056	8220	8079	7487	7706	7881	7560	7815	7496	8580
	20 iterations	8256	8492	8101	8276	8137	7522	7750	7920	7555	7853	7501	8620
	4mm	7914	8248	7647	7950	7768	7182	7384	7809	7532	7565	7199	8140
	Default	7141	7194	6768	8023	8213	7356	6118	6848	8198	7923	8361	7551
	3 iterations	7299	7399	7053	8133	8172	7562	6520	7156	8290	8506	8394	7850
	4 iterations	7675	7721	7680	8543	8059	7854	7073	7466	8761	9046	8907	8387
TOF	6 iterations	8539	8179	8396	9129	8372	8321	7694	7912	9222	9520	9423	8910
BLAD40	10 iterations	9471	8601	8966	9656	9038	8843	8192	8311	9472	9789	9721	9218
	20 iterations	9817	8850	9363	10000	9442	9281	8563	8515	9551	9914	9819	9330
	4mm	7509	7511	7118	8480	8285	7624	6399	7080	8821	8534	9056	8120
	Default	7042	6504	6181	7571	9118	7103	5724	6713	8207	7111	7734	7442
	3 iterations	7108	6763	6545	7759	8969	7361	5937	6953	8286	7271	7926	7796
	4 iterations	7343	6991	7286	8055	8657	7502	6539	7193	8780	7857	8341	8421
TOF	6 iterations	8128	7439	8200	8642	8900	7787	7296	7614	9280	8518	8820	9073
BLAD80	10 iterations	9239	7997	8980	9403	9823	8162	7917	8093	9531	8991	9141	9481
	20 iterations	9832	8424	9648	10105	10645	8588	8238	8535	9558	9201	9211	9635
	4mm	7283	6734	6430	7834	9167	7170	5907	6945	8756	7539	8123	7994

Table A.7: Mean Values of SBG for D690 Ga68

mean		SBG01	SBG02	SBG03	SBG04	SBG05	SBG06	SBG07	SBG08	SBG09	SBG10	SBG11	SBG12
	Default	3870	4371	4544	3586	3831	4538	4379	3488	3493	3742	3703	3756
	3 iterations	3885	4433	4566	3569	3798	4440	4292	3475	3474	3728	3720	3833
	4 iterations	3850	4353	4490	3538	3821	4343	4191	3438	3369	3673	3674	3778
nTOF	6 iterations	3817	4210	4337	3518	3888	4161	4019	3423	3219	3584	3617	3693
BLAD1	10 iterations	3815	4053	4156	3538	4017	3939	3839	3474	3066	3491	3601	3607
	20 iterations	3830	3952	4006	3576	4137	3745	3729	3581	2977	3436	3699	3532
	4mm	3836	4380	4549	3546	3844	4508	4356	3471	3456	3738	3698	3735
	Default	7421	4199	4944	7855	8288	5172	4326	9146	4605	4214	4507	5026
	3 iterations	7064	4181	4870	7534	7898	5169	4337	8724	4669	4211	4453	4970
	4 iterations	6402	4290	5026	6925	7071	5351	4374	7979	4661	4102	4420	4972
nTOF	6 iterations	5729	4344	5106	6362	6250	5522	4374	7324	4648	3922	4385	4949
BLAD40	10 iterations	5195	4234	4926	6031	5645	5493	4230	6971	4658	3696	4392	4881
	20 iterations	4914	4058	4539	6005	5360	5243	3969	6948	4728	3516	4495	4752
	4mm	7262	4144	4912	7765	8029	5101	4101	9065	4585	4160	4509	5032
	Default	8424	3399	4657	8685	9913	5082	4266	10075	4425	4423	4415	4701
	3 iterations	7932	3332	4604	8283	9398	5062	4207	9463	4424	4349	4388	4698
	4 iterations	7155	3415	4882	7452	8342	5353	4314	8541	4422	4313	4329	4648
nTOF	6 iterations	6383	3497	5223	6636	7334	5757	4469	7708	4409	4237	4239	4558
BLAD80	10 iterations	5763	3438	5298	5999	6618	5991	4488	7181	4380	4116	4125	4436
	20 iterations	5364	3241	4921	5547	6220	5851	4242	6956	4381	4032	4014	4347
	4mm	8247	3331	4594	8511	9623	4974	4002	9880	4446	4397	4359	4647
	Default	3386	3503	3781	3460	3495	3850	3369	3217	2955	3226	2966	3190
	3 iterations	3399	3543	3777	3511	3462	3780	3334	3244	2935	3155	2971	3231
	4 iterations	3359	3442	3686	3546	3490	3669	3220	3282	2875	3125	2892	3196
TOF	6 iterations	3325	3326	3587	3619	3551	3532	3097	3363	2814	3114	2798	3165
BLAD1	10 iterations	3303	3240	3529	3696	3615	3419	3015	3455	2783	3133	2714	3153
	20 iterations	3288	3207	3527	3723	3657	3389	2999	3502	2825	3176	2673	3169
	4mm	3315	3498	3771	3464	3508	3817	3320	3218	2914	3240	2920	3181
	Default	5461	4618	5329	5143	5634	5539	4802	5928	4365	3909	4223	4842
	3 iterations	5263	4496	5166	4924	5420	5457	4797	5723	4327	3897	4160	4755
	4 iterations	4941	4449	5107	4606	4994	5419	4729	5389	4287	3778	4114	4771
TOF	6 iterations	4622	4309	4937	4330	4614	5283	4582	5143	4258	3639	4097	4795
BLAD40	10 iterations	4389	4112	4690	4184	4399	5058	4370	5082	4269	3546	4147	4811
	20 iterations	4337	3983	4468	4151	4446	4840	4211	5200	4357	3590	4245	4803
	4mm	5359	4569	5288	5036	5425	5446	4588	5859	4347	3857	4227	4880
	Default	5713	4073	5562	5403	6362	5680	5060	5817	4244	4291	4646	4684
	3 iterations	5441	3934	5358	5180	6039	5546	4937	5466	4192	4162	4597	4667
	4 iterations	5053	3905	5373	4720	5442	5546	4941	4967	4137	4081	4557	4613
TOF	6 iterations	4677	3802	5250	4275	4881	5437	4884	4504	4085	3987	4530	4548
BLAD80	10 iterations	4382	3619	4939	3925	4446	5154	4707	4181	4083	3931	4535	4498
	20 iterations	4290	3455	4546	3724	4165	4730	4457	4060	4156	3957	4555	4498
	4mm	5587	3987	5525	5259	6088	5556	4786	5665	4265	4281	4615	4660

Table A.8: Mean Values of LBG & BLADDER for D690 Ga68

mean		LBG	BLADDER	mean		LBG	BLADDER
	Default	3380	3849		Default	3325	3231
	3 iterations	3387	3856		3 iterations	3331	3240
	4 iterations	3394	3862		4 iterations	3330	3271
nTOF	6 iterations	3401	3882	TOF	6 iterations	3329	3317
BLAD1	10 iterations	3404	3921	BLAD1	10 iterations	3329	3349
	20 iterations	3403	3963		20 iterations	3329	3355
	4mm	3382	3860		4mm	3327	3242
	Default	3965	134689		Default	3839	135300
	3 iterations	3968	134733		3 iterations	3845	135100
	4 iterations	3979	135020		4 iterations	3849	135144
nTOF	6 iterations	3989	135273	TOF	6 iterations	3851	135207
BLAD40	10 iterations	3994	135431	BLAD40	10 iterations	3851	135245
	20 iterations	3994	135474		20 iterations	3852	135247
	4mm	3967	135211		4mm	3841	135836
	Default	3776	241441		Default	3626	240988
	3 iterations	3782	241640		3 iterations	3630	240834
	4 iterations	3796	242184		4 iterations	3635	240996
nTOF	6 iterations	3806	242688	TOF	6 iterations	3637	241165
BLAD80	10 iterations	3811	242997	BLAD80	10 iterations	3638	241255
	20 iterations	3811	243091		20 iterations	3638	241268
	4mm	3778	242660		4mm	3627	242263

Table A.9: Max Values of SL for DIQ F18

max		SL01	SL02	SL03	SL04	SL05	SL06	SL07	SL08	SL09	SL10	SL11	SL12
	3 iterations	6679	7617	7974	7596	7365	6813	7941	7069	6849	7672	5933	7465
	Default	7588	8602	8897	8541	8330	7502	8788	7842	7583	8625	6629	8348
OSEM	4 iterations	9149	10160	10183	9939	9835	8486	9985	8989	8728	10014	7823	9625
BLAD1	10 iterations	11124	11982	11470	11330	11534	9476	11277	10185	10053	11430	9366	10983
	20 iterations	12642	13462	12608	12141	12907	10091	12430	10932	11019	12461	10657	12287
	4mm	9106	10034	10313	9482	9306	8516	9820	8491	8488	9906	7535	9708
	3 iterations	11611	8476	5546	7849	14746	9618	5304	9298	10846	6002	9190	6101
	Default	10583	8815	6581	8074	12992	9843	6071	8793	12123	6797	9129	6809
OSEM	4 iterations	10175	9622	8433	8818	11781	10591	7608	8905	14102	8191	9997	7930
BLAD40	10 iterations	11094	10941	10641	9888	11689	11937	9727	10155	16307	10053	10911	9285
	20 iterations	14284	12534	12249	11030	14081	13711	11528	11546	17840	11653	12038	10611
	4mm	11730	9823	7358	8839	12725	10930	6617	8772	13947	7826	9827	7430
	3 iterations	13735	8612	4041	8194	18029	10918	4098	9929	11208	5231	10269	5180
	Default	12043	8335	4636	7754	15320	10515	4552	9027	11018	5843	9548	5794
OSEM	4 iterations	10468	8745	6115	8368	13056	10967	5753	8144	12488	6963	8706	6913
BLAD80	10 iterations	10240	9881	8505	9567	12395	12099	8308	8719	14731	8576	9552	8555
	20 iterations	12591	11621	10924	10719	13921	13962	11590	10494	17340	10132	10687	10426
	4mm	12629	9019	5037	8098	14925	11687	5146	9071	12584	6343	9405	6283
REG	Default	6844	7927	8476	7947	8381	7251	7939	7534	8076	7956	6377	8381
BLAD1	β=150	11000	11819	13357	12050	12840	10477	11725	10711	11745	12489	9355	13120
REG	Default	5867	7461	7728	7297	8471	7921	7147	6916	10038	6443	7486	6889
BLAD40	β=150	7563	10960	11467	9724	10563	10940	10812	9340	16719	9942	10333	10040
REG	Default	5943	6222	6321	6300	8404	7806	5561	6111	8578	5299	6497	5650
BLAD80	β=150	6812	8350	9612	8430	9197	10815	8095	7525	12927	8465	7910	8334

Table A.10: Mean Values of SL for DIQ F18

mean		SL01	SL02	SL03	SL04	SL05	SL06	SL07	SL08	SL09	SL10	SL11	SL12
	3 iterations	5331	6164	6266	5936	6256	5677	6592	6014	5863	5852	4910	5902
	Default	5764	6667	6705	6371	6855	6065	7068	6497	6309	6297	5257	6319
OSEM	4 iterations	6465	7405	7291	6984	7757	6602	7691	7214	6982	6918	5831	6878
BLAD1	10 iterations	7314	8188	7905	7598	8748	7137	8304	8002	7748	7537	6552	7437
	20 iterations	8007	8741	8519	8010	9567	7511	8813	8618	8351	7974	7167	7943
	4mm	6131	7075	7108	6767	7315	6391	7485	6870	6644	6694	5520	6662
	3 iterations	9067	7229	4371	6682	11341	8388	4747	7361	8552	4975	7515	4942
	Default	8170	7358	4944	6842	10317	8436	5271	7363	9093	5390	7844	5361
OSEM	4 iterations	7422	7728	5952	7219	9513	8724	6352	7585	9899	6061	8363	6027
BLAD40	10 iterations	7305	8312	7089	7744	9542	9225	7855	8060	10749	6849	8988	6814
	20 iterations	8179	8995	7911	8338	10880	9794	9085	8655	11331	7426	9490	7527
	4mm	8449	7652	5147	6991	10476	8760	5487	7518	9593	5706	8159	5620
	3 iterations	10965	7128	3543	6578	13114	9183	3668	7285	8509	4202	7126	4136
	Default	9658	7072	3971	6619	11511	9038	3892	7030	8862	4527	7132	4450
OSEM	4 iterations	8468	7284	4885	6927	10073	9193	4548	6963	9490	5154	7252	5035
BLAD80	10 iterations	7944	7829	6201	7442	9488	9717	5821	7231	10372	6098	7572	5847
	20 iterations	8700	8625	7257	7959	10445	10388	7196	7863	11226	7156	8001	6602
	4mm	9925	7285	4053	6667	11423	9309	3925	7092	9268	4733	7289	4627
REG	Default	5698	6595	6693	6413	6931	5987	6624	6450	6743	6097	5293	6439
BLAD1	β=150	7366	8398	8762	8281	9383	7543	8516	8270	8680	7910	6671	8126
REG	Default	5055	6523	6400	6397	7080	6984	6183	6238	8011	5437	6686	5777
BLAD40	β=150	5826	8319	8150	7649	8728	8589	8436	7636	10851	6915	8413	7284
REG	Default	5150	5650	5643	5741	7053	7123	4716	5379	7323	4490	5495	4731
BLAD80	β=150	5553	6884	7478	6746	8032	8888	6161	6227	9653	6177	6386	6043

Table A.11: Mean Values of SBG for DIQ F18

mean		SBG01	SBG02	SBG03	SBG04	SBG05	SBG06	SBG07	SBG08	SBG09	SBG10	SBG11	SBG12
	3 iterations	3963	4328	4531	3804	4021	4729	4322	3523	4232	3797	3916	4058
	Default	3958	4258	4507	3751	4037	4771	4261	3481	4226	3717	3885	4027
OSEM	4 iterations	3950	4099	4391	3664	4062	4745	4107	3443	4187	3575	3820	3965
BLAD1	10 iterations	3980	3883	4186	3572	4130	4608	3872	3459	4128	3401	3746	3907
	20 iterations	4097	3734	3998	3501	4277	4402	3635	3559	4083	3250	3701	3900
	4mm	3903	4231	4503	3709	4034	4780	4252	3475	4250	3667	3895	4036
	3 iterations	7674	4202	4698	7111	8661	5089	4045	8307	4438	4673	4131	4819
	Default	6903	4366	4949	6444	7646	5081	3974	7253	4448	4730	4100	4851
OSEM	4 iterations	6055	4611	5269	5726	6562	5164	3918	6141	4438	4808	4040	4862
BLAD40	10 iterations	5292	4764	5358	5102	5645	5259	3766	5231	4387	4892	3946	4810
	20 iterations	4717	4772	5079	4677	4979	5250	3383	4606	4305	4993	3851	4663
	4mm	6834	4370	4968	6354	7359	4962	3742	7147	4471	4807	4112	4826
	3 iterations	8889	3659	4616	8681	10504	5132	4058	10425	4196	4384	3906	5031
	Default	7832	3760	4902	7848	9093	5017	3951	9013	4208	4376	3823	5159
OSEM	4 iterations	6686	4021	5430	7021	7594	5027	3934	7548	4254	4376	3703	5391
BLAD80	10 iterations	5630	4306	5891	6367	6300	5136	3971	6348	4328	4349	3525	5722
	20 iterations	4666	4331	5843	5933	5223	5108	3849	5438	4442	4257	3296	6139
	4mm	7727	3729	4935	7797	8608	4701	3611	8851	4229	4364	3746	5196
REG	Default	3835	4016	4248	3684	4034	4654	4108	3513	4049	3430	3743	3852
BLAD1	β=150	3788	3753	4071	3564	4157	4656	3940	3524	4053	3232	3727	3857
REG	Default	4530	4718	5301	4566	5045	5007	3944	4649	4164	4435	3819	4764
BLAD40	β=150	4216	4752	5332	4381	4603	5153	3647	4277	4222	4628	3780	4794
REG	Default	4667	4195	5376	5293	5416	4549	3544	5547	3862	4095	3605	5042
BLAD80	β=150	4209	4291	5679	5302	4669	4667	3492	5130	4079	4071	3423	5571

Table A.12: Mean Values of LBG & BLADDER for DIQ F18

mean		LBG	BLADDER
OSEM BLAD1	3 iterations	3834	3578
	Default	3851	3540
	4 iterations	3870	3491
	10 iterations	3888	3456
	20 iterations	3896	3453
	4mm	3856	3543
OSEM BLAD40	3 iterations	4175	165338
	Default	4196	165853
	4 iterations	4218	166289
	10 iterations	4236	166612
	20 iterations	4248	166839
	4mm	4201	166774
OSEM BLAD80	3 iterations	3948	314942
	Default	3974	315656
	4 iterations	4001	316347
	10 iterations	4020	316918
	20 iterations	4033	317348
	4mm	3979	317580
REG BLAD1	Default	3887	3455
	=150	3886	3466
REG BLAD40	Default	4228	170294
	=150	4228	169064
REG BLAD80	Default	4012	323857
	=150	4014	321948

Table A.13: Max Values of SL for DIQ Ga68

max		SL01	SL02	SL03	SL04	SL05	SL06	SL07	SL08	SL09	SL10	SL11	SL12
OSEM BLAD1	3 iterations	5343	5423	5989	5982	4759	5705	5404	5693	5544	5693	5311	4972
	Default	5980	5910	6567	6620	5149	6331	5804	6288	6145	6293	5885	5379
	4 iterations	7057	6635	7378	7576	5748	7275	6373	7171	7113	7201	6813	5995
	10 iterations	8410	7420	8278	8662	6511	8317	7036	8138	8306	8222	7986	6758
	20 iterations	9453	8007	9164	9555	7205	9042	7715	8964	9351	9058	9099	7558
	4mm	6949	6502	7263	7180	5539	6901	6340	6916	6856	6938	6455	5808
OSEM BLAD40	3 iterations	10422	7021	4748	7999	13958	9239	4654	8022	8806	5997	7427	5633
	Default	9662	7218	5504	8050	12432	8975	5382	7522	9170	6782	8067	6299
	4 iterations	9152	7744	6768	8565	10879	9415	6885	7608	10127	8036	9198	7355
	10 iterations	9383	8730	8232	9482	10808	10126	9004	8445	11436	9812	10520	8598
	20 iterations	11036	10186	9250	10790	12962	10647	10562	9989	12809	11307	11570	9764
	4mm	10278	7814	6023	8813	12132	9821	6095	8083	10090	7596	8989	6880
OSEM BLAD80	3 iterations	11374	7539	3348	8442	17115	11552	3893	10035	9928	4174	8223	4284
	Default	10202	7229	3797	8055	14849	10881	3917	9443	9469	4635	8379	4806
	4 iterations	9196	7084	4754	8023	12556	10379	4097	9048	9055	5577	8774	5793
	10 iterations	8914	7510	6142	8709	10925	10249	5544	9487	9841	7095	9471	7323
	20 iterations	9975	8704	7167	10098	12130	10707	8238	11376	11238	8729	10574	9318
	4mm	10490	7361	3885	8412	14434	10498	3363	9281	10017	5181	9021	5279
REG BLAD1	Default	5540	5806	6356	6927	5225	5970	5273	5906	6052	6026	5809	5894
	β=150	8177	7923	8888	9944	6644	8444	6848	8210	8702	8338	8085	8008
REG BLAD40	Default	6171	5835	6411	6469	8649	7468	6051	6046	7300	6807	7033	6790
	β=150	7528	7820	8616	9011	9140	10227	9703	7909	11204	10642	10114	9983
REG BLAD80	Default	6014	5282	4858	5888	8719	6806	3866	6053	6693	4496	6765	4697
	β=150	6852	6965	6317	8123	8328	7959	5170	7406	9225	6619	8541	7363

Table A.14: Mean Values of SL for DIQ Ga68

mean		SL01	SL02	SL03	SL04	SL05	SL06	SL07	SL08	SL09	SL10	SL11	SL12
	3 iterations	4478	4740	5029	5181	4310	4788	4761	4740	4744	4739	4491	4345
	Default	4820	5035	5334	5600	4578	5154	4997	5062	5098	5061	4821	4584
OSEM	4 iterations	5363	5459	5722	6209	4985	5685	5308	5514	5646	5521	5329	4928
BLAD1	10 iterations	5990	5912	6099	6882	5459	6261	5633	5972	6285	6008	5919	5342
	20 iterations	6438	6225	6412	7455	5869	6732	5915	6297	6782	6373	6370	5799
	4mm	5099	5267	5596	5914	4750	5437	5226	5314	5355	5304	5010	4767
	3 iterations	8094	6044	3798	6235	10388	7925	3958	6603	7273	4707	6242	4472
	Default	7407	6101	4263	6322	9409	7871	4357	6518	7536	5150	6561	4865
OSEM	4 iterations	6856	6340	5053	6573	8558	7978	5193	6598	7987	5876	7032	5480
BLAD40	10 iterations	6772	6794	5911	6955	8288	8207	6355	6930	8588	6712	7525	6170
	20 iterations	7282	7404	6490	7417	8814	8399	7266	7503	9180	7304	7864	6762
	4mm	7501	6320	4383	6446	9516	8050	4517	6656	7902	5394	6790	5056
	3 iterations	8877	6005	2773	6080	11905	8009	2751	6801	6920	3412	5868	3259
	Default	7920	5925	3060	6086	10423	7700	2860	6529	7006	3619	6079	3469
OSEM	4 iterations	7063	6020	3697	6353	9026	7592	3250	6417	7232	4042	6435	3887
BLAD80	10 iterations	6708	6306	4670	6918	8246	7788	4115	6604	7678	4689	6932	4538
	20 iterations	7257	6725	5658	7746	8532	8119	5458	6978	8322	5359	7526	5357
	4mm	8041	5998	3073	6145	10480	7745	2824	6546	7278	3757	6305	3582
REG	Default	4777	5040	5405	5830	4760	5115	4693	5009	5187	5127	4825	4914
BLAD1	β=150	6082	6217	6576	7465	5687	6500	5585	6185	6592	6296	6071	5904
REG	Default	5042	5302	5332	5648	6746	6710	5043	5493	6367	5441	5997	5329
BLAD40	β=150	5804	6416	6575	6827	7547	7989	6797	6536	8323	7156	7287	6806
REG	Default	4769	4751	4417	5215	6044	5784	3396	4972	5611	3711	5273	3847
BLAD80	β=150	5299	5609	5513	6418	6568	6846	4137	5853	7232	4622	6375	4827

Table A.15: Mean Values of SBG for DIQ Ga68

mean		SBG01	SBG02	SBG03	SBG04	SBG05	SBG06	SBG07	SBG08	SBG09	SBG10	SBG11	SBG12
	3 iterations	3145	3695	3900	3111	2944	3708	3888	2928	3241	3253	3392	3067
	Default	3109	3673	3893	3065	2892	3713	3927	2886	3203	3218	3400	2993
OSEM	4 iterations	3051	3595	3801	3002	2811	3660	3935	2837	3128	3143	3389	2868
BLAD1	10 iterations	2999	3479	3608	2951	2726	3524	3896	2822	3034	3030	3350	2708
	20 iterations	2987	3402	3373	2941	2678	3321	3822	2885	2951	2908	3279	2524
	4mm	3063	3657	3877	3007	2853	3684	3958	2853	3195	3250	3405	2977
	3 iterations	6705	3592	4285	7392	8307	4890	4940	8286	3930	4118	3925	4774
	Default	6076	3656	4516	6647	7343	4862	4890	7327	3925	4117	3915	4837
OSEM	4 iterations	5413	3753	4828	5867	6294	4905	4890	6312	3921	4092	3910	4913
BLAD40	10 iterations	4856	3768	4965	5247	5395	4948	4859	5473	3914	4004	3923	4971
	20 iterations	4451	3635	4791	4900	4782	4959	4682	4876	3911	3870	3995	5015
	4mm	5979	3586	4469	6403	7072	4517	4424	7270	3947	4087	3969	4824
	3 iterations	7677	3063	3606	8748	9485	4864	5048	9643	3325	3837	3130	4464
	Default	6852	3062	3740	7768	8102	4751	4868	8412	3228	3847	2982	4517
OSEM	4 iterations	5995	3129	4050	6777	6606	4753	4742	7123	3097	3887	2775	4622
BLAD80	10 iterations	5253	3162	4364	5991	5292	4854	4669	6054	2920	3929	2512	4771
	20 iterations	4601	2945	4287	5430	4217	4846	4528	5242	2659	3912	2202	4946
	4mm	6771	2964	3653	7457	7631	4109	4033	8363	3168	3875	2950	4501
REG	Default	3045	3510	3652	3103	2832	3604	3749	2907	3106	2931	3134	2852
BLAD1	β=150	2917	3423	3485	3022	2706	3531	3805	2878	3066	2853	3170	2712
REG	Default	4201	3947	4867	4514	4839	4546	4021	4883	3652	3763	3549	4544
BLAD40	β=150	3998	3884	4979	4227	4221	4404	3841	4558	3665	3712	3659	4691
REG	Default	4366	3185	4158	4895	4412	3953	3476	5028	2844	3488	2409	4297
BLAD80	β=150	4192	3023	4338	4781	3608	3945	3241	4673	2699	3530	2115	4577

Table A.16: Mean Values of LBG & BLADDER for DIQ Ga68

mean		LBG	BLADDER
OSEM BLAD1	3 iterations	3174	3049
	Default	3188	3030
	4 iterations	3204	3006
	10 iterations	3218	2993
	20 iterations	3225	3008
	4mm	3192	3033
OSEM BLAD40	3 iterations	3775	141048
	Default	3793	141465
	4 iterations	3812	141813
	10 iterations	3827	142050
	20 iterations	3835	142194
	4mm	3798	142162
OSEM BLAD80	3 iterations	3471	257172
	Default	3493	257862
	4 iterations	3516	258500
	10 iterations	3533	258978
	20 iterations	3543	259291
	4mm	3497	259426
REG BLAD1	Default	3214	2967
	=150	3213	2994
REG BLAD40	Default	3815	144719
	=150	3816	143929
REG BLAD80	Default	3520	264085
	=150	3520	262914

Bibliography

[1] Brownell, G. L., & Sweet, W. H. (1953). Localization of brain tumors with positron emitters. *Nucleonics, 11*(11), 40-45.

[2] Rankowitz, S., Robertson, J. S., Higinbotham, W. A., & Rosenblum, M. J. (1961). *Positron scanner for locating brain tumors* (No. BNL-6041). Brookhaven National Lab.,(BNL) Upton, NY.

[3] Phelps, M. E., Hoffman, E. J., Mullani, N. A., & Ter-Pogossian, M. M. (1975). Application of annihilation coincidence detection to transaxial reconstruction tomography. *Journal of Nuclear Medicine, 16*(3), 210-224.

[4] Ter-Pogossian, M. M., Phelps, M. E., Hoffman, E. J., & Mullani, N. A. (1975). A positron-emission transaxial tomograph for nuclear imaging (PETT). *Radiology, 114*(1), 89-98.

[5] Cho, Z. H., & Farukhi, M. R. (1977). Bismuth germanate as a potential scintillation detector in positron cameras. *J Nucl Med, 18*(8), 840-4.

[6] Beyer, T., Townsend, D. W., Brun, T., & Kinahan, P. E. (2000). A combined PET/CT scanner for clinical oncology. *The Journal of nuclear medicine, 41*(8), 1369.

[7] Cherry, S. R., Sorenson, J., Phelps, M. E., & Methe, B. M. (2004). Physics in nuclear medicine. *Medical Physics, 31*(8), 2370-2371.

[8] Dempster, A. P., Laird, N. M., & Rubin, D. B. (1977). Maximum likelihood from incomplete data via the EM algorithm. *Journal of the royal statistical society. Series B (methodological)*, 1-38.

[9] Hudson, H. M., & Larkin, R. S. (1994). Accelerated image reconstruction using ordered subsets of projection data. *IEEE transactions on medical imaging, 13*(4), 601-609.

[10] Ross, S. (2014). Q. Clear. *GE Healthcare, White Paper*, 1-9.

[11] Pacák, J., Točík, Z., & Černý, M. (1969). Synthesis of 2-deoxy-2-fluoro-D-glucose. *Journal of the Chemical Society D: Chemical Communications*, (2), 77-77.

[12] Ido, T., Wan, C. N., Casella, V., Fowler, J. S., Wolf, A. P., Reivich, M., & Kuhl, D. E. (1978). Labeled 2-deoxy-D-glucose analogs. 18F-labeled 2-deoxy-2-fluoro-D-glucose, 2-deoxy-2-fluoro-D-mannose and 14C-2-deoxy-2-fluoro-D-glucose. *Journal of Labelled Compounds and Radiopharmaceuticals, 14*(2), 175-183.

[13] Al-Nahhas, A., Win, Z., Szyszko, T., Singh, A., Nanni, C., Fanti, S., & Rubello, D. (2007). *Gallium-68 PET: a new frontier in receptor cancer imaging. Anticancer research, 27*(6B), 4087-4094.

[14] Stetter, H., & Frank, W. (1976). Complex Formation with Tetraazacycloalkane-N, N, N , N-tetraacetic Acids as a Function of Ring Size. *Angewandte Chemie International Edition, 15*(11), 686-686.

[15] Knör, S., Modlinger, A., Poethko, T., Schottelius, M., Wester, H. J., & Kessler, H. (2007). Synthesis of Novel 1, 4, 7, 10-Tetraazacyclodecane-1, 4, 7, 10-Tetraacetic Acid (DOTA) Derivatives for Chemoselective Attachment to Unprotected Polyfunctionalized Compounds. *Chemistry-a European Journal, 13*(21), 6082-6090.

[16] Shastry, M., Kayani, I., Wild, D., Caplin, M., Visvikis, D., Gacinovic, S., ... & Bomanji, J. B. (2010). Distribution pattern of ^{68}Ga-DOTATATE in disease-free patients. *Nuclear medicine communications, 31*(12), 1025-1032.

[17] Kuyumcu, S., Özkan, Z. G., Sanli, Y., Yilmaz, E., Mudun, A., Adalet, I., & Unal, S. (2013). Physiological and tumoral uptake of ^{68}Ga-DOTATATE: standardized uptake values and challenges in interpretation. *Annals of nuclear medicine, 27*(6), 538-545.

[18] Moradi, F., Jamali, M., Barkhodari, A., Schneider, B., Chin, F., Quon, A., ... & Iagaru, A. (2016). Spectrum of ^{68}Ga-DOTA TATE Uptake in Patients With Neuroendocrine Tumors. *Clinical nuclear medicine, 41*(6), e281-e287.

[19] Rufini, V., Calcagni, M. L., & Baum, R. P. (2006, July). Imaging of neuroendocrine tumors. In *Seminars in nuclear medicine* (Vol. 36, No. 3, pp. 228-247). WB Saunders.

[20] Moradi, F., Jamali, M., Barkhodari, A., Schneider, B., Chin, F., Quon, A., ... & Iagaru, A. (2016). Spectrum of 68Ga-DOTA TATE uptake in patients with neuroendocrine tumors. *Clinical nuclear medicine, 41*(6), e281-e287.

[21] Allen, C. (2012). *SUV Analysis of F-18 FDG PET Imaging in the Vicinity of the Bladder* (Doctoral dissertation).

[22] Gofrit, O. N., Frank, S., Meirovitz, A., Nechushtan, H., & Orevi, M. (2017). PET/CT with 68Ga-DOTA-TATE for diagnosis of Neuroendocrine: differentiation in patients with castrate-resistant prostate cancer. *Clinical nuclear medicine, 42*(1), 1-6.

[23] Usmani, S., Ahmed, N., Marafi, F., Rasheed, R., Amanguno, H. G., & Al, F. K. (2017). Molecular Imaging in Neuroendocrine Differentiation of Prostate Cancer: 68Ga-PSMA Versus 68Ga-DOTA NOC PET-CT. *Clinical nuclear medicine, 42*(5), 410-413.

[24] Berliner, C., Tienken, M., Frenzel, T., Kobayashi, Y., Helberg, A., Kirchner, U., ... & Mester, J. (2017). Detection rate of PET/CT in patients with biochemical relapse of prostate cancer using [68 Ga] PSMA I&T and comparison with published data of [68 Ga] PSMA HBED-CC. *European journal of nuclear medicine and molecular imaging, 44*(4), 670-677.

[25] Nayyeri, F., Rahni, A. A. A., & Ab Aziz, A. (2015, October). Modelling the GE discovery 690 PET/CT scanner. In *Signal and Image Processing Applications (ICSIPA), 2015 IEEE International Conference on* (pp. 160-164). IEEE.

[26] Reynés-Llompart, G., Gámez-Cenzano, C., Romero-Zayas, I., Rodríguez-Bel, L., Vercher-Conejero, J. L., & Martí-Climent, J. M. (2017). Performance characteristics of the whole-body discovery IQ PET/CT system. *Journal of Nuclear Medicine, 58*(7), 1155-1161.

[27] Moradi, F., Jamali, M., Barkhodari, A., Schneider, B., Chin, F., Quon, A., ... & Iagaru, A. (2016). Spectrum of 68Ga-DOTA TATE uptake in patients with neuroendocrine tumors. *Clinical nuclear medicine, 41*(6), e281-e287.

[28] Lodge, M. A., Chaudhry, M. A., Udall, D. N., & Wahl, R. L. (2010). Characterization of a perirectal artifact in 18F-FDG PET/CT. *Journal of Nuclear Medicine, 51*(10), 1501-1506.

[29] Al-Nahhas, A., Win, Z., Szyszko, T., Singh, A., Nanni, C., Fanti, S., & Rubello, D. (2007). Gallium-68 PET: a new frontier in receptor cancer imaging. *Anticancer research, 27*(6B), 4087-4094.

[30] Leisure, G. P., Vesselle, H. J., Faulhaber, P. F., ODonnell, J. K., Adler, L. P., & Miraldi, F. (1997). Technical improvements in fluorine-18-FDG PET imaging of the abdomen and pelvis. *Journal of nuclear medicine technology, 25*(2), 115-119.

[31] Koyama, K., Okamura, T., Kawabe, J., Ozawa, N., Torii, K., Umesaki, N., ... & Yamada, R. (2003). Evaluation of 18F-FDG PET with bladder irrigation in patients with uterine and ovarian tumors. *Journal of Nuclear Medicine, 44*(3), 353-358.

[32] Lin, W. Y., Hung, G. U., & Tsai, S. C. (2005). A pitfall of FDG-PET image interpretation: accumulation of FDG in the dependent area of the urinary bladder after bladder irrigation–the usefulness of the prone position. *Clinical nuclear medicine, 30*(9), 638-639.

[33] Lin, W. Y., Wang, K. B., Tsai, S. C., & Sun, S. S. (2009). Unexpected accumulation of F-18 FDG in the urinary bladder after bladder irrigation and retrograde filling with sterile saline: a possible pitfall in PET examination. *Clinical nuclear medicine, 34*(9), 560-563.

[34] Anjos, D. A., Etchebehere, E. C., Ramos, C. D., Santos, A. O., Albertotti, C., & Camargo, E. E. (2007). 18F-FDG PET/CT delayed images after diuretic for restaging invasive bladder cancer. *Journal of Nuclear Medicine, 48*(5), 764-770.

[35] Harkirat, S., Anand, S. S., & Jacob, M. J. (2010). Forced diuresis and dual-phase 18F-fluorodeoxyglucose-PET/CT scan for restaging of urinary bladder cancers. *The Indian journal of radiology & imaging, 20*(1), 13.

[36] Capasso, E., Durzu, S., Piras, S., Zandieh, S., Knoll, P., Haug, A., ... & Mirzaei, S. (2015). Role of 64 CuCl 2 PET/CT in staging of prostate cancer. *Annals of nuclear medicine, 29*(6), 482-488.

[37] Piccardo, A., Paparo, F., Puntoni, M., Righi, S., Bottoni, G., Bacigalupo, L., ... & Ruggieri, F. G. (2018). 64CuCl2 PET/CT in prostate cancer relapse. *Journal of Nuclear Medicine, 59*(3), 444-451.